Laporte-Azcué, M., González-Gómez, P. A., Rodríguez-Sánchez, M. R. & Santana, D. (2020). Exergy analysis of solar central receivers. *Solar Energy*, 207, pp. 957–973.

DOI: 10.1016/j.solener.2020.07.033

Exergy analysis of solar central receivers

M. Laporte-Azcué*, P.A. González-Gómez, M.R. Rodríguez-Sánchez, D. Santana

Energy Systems Engineering Group (ISE), Department of Thermal and Fluid Engineering, University Carlos III of Madrid, Av. Universidad 30, 28911.

* mlaporte@ing.uc3m.es

Abstract

A high-resolution method to analyse the exergy of the SPT external tubular receivers is presented, examining the different heat transfer process involved individually. This sheds light on the role that each irreversibility source plays in the outcome, aiding in the receiver design and the facility location selection. The exergy efficiency is around 32% in the base configuration. Besides the exergy loss in the heliostat field, over 40%, it is found that the biggest exergy destruction cause are the radiation emissions and absorptions in the tube outer surface, around 17%. From the remaining ones, the greatest are the exergy destructed in the HTF and the one escaping to the ambient (over 4% each). Then, the exergy balance for a variety of strategies and ambient conditions is performed: optical properties of the tubes coating, peak and flat aiming strategies, DNI and ambient temperature. The heliostat field exergy loss rate only varies when changing the aiming. However, the emission and absorption losses and the ones in the HTF suffer the greater modifications with all the parameters studied. The impact of the optical properties degradation, 1% descent in the efficiency per 5% degradation, would advise repainting works in order to avoid greater exergy destruction. The surroundings temperature modification impacts considerably the exergy efficiency, showing the suitability of locations with low ambient temperature and a moderate DNI: descends of over 0.35% occur every 5 °C increase of the temperature for a fixed DNI.

Keywords:
Solar power tower; External central receiver; Exergy efficiency; Radiation; Heat transfer.

Nomenclature

a_1: elbow angle coefficient

A: surface area (m^2), absorptivity matrix

C: cross-section area (m^2)

Cp: heat capacity ($J\ kg^{-1}\ K^{-1}$)

cr: corrosion ratio ($m\ year^{-1}$)

d: duct diameter (m)

D: receiver diameter (m)

DNI: direct normal irradiation ($W\ m^{-2}$)

E: emission (W), emission matrix

E_1: joint efficiency factor coefficient

fr: Darcy friction factor

F: view factor

h: axial division counter, convective heat transfer coefficient ($W\ m^{-2}\ K^{-1}$)

k: thermal conductivity ($W\ m^{-1}\ K^{-1}$)

K: expansion or contraction resistance coefficient

L: length of the duct (m)

lc: lifecycle of the plant (years)

m: total of axial divisions in one flow path

$\dot{m}$: mass flow (kg s^{-1})

n: total number of circumferential divisions in half the cross-section

N_{fp}: number of flow paths for the HTF

N_p: number of panels in the receiver

N_t: number of tubes

p: perimeter (m)

q: heat flux (W m^{-2})

Q: heat (W)

R: reflectivity matrix, resistance

R_0: elbows curvature radius (m)

Re: Reynolds number

T: temperature (K)

TOL: admissible calculation tolerance in the iterative process

th: thickness (m)

U: overall heat transfer coefficient (W m^{-2} K^{-1})

X: exergy (W)

z: axial coordinate

Greek symbols

α: absorptivity

ΔP: pressure drop (Pa)

ΔS_{gen}: entropy generation (WK^{-1})

ΔT: temperature difference (K)

Δz: height of the axial divisions (m)

ε: emissivity

η: efficiency (%)

ξ: percentage of exergy loss (%)

ρ: reflectivity, HTF density (kg m^{-3})

σ: Stefan-Boltzmann constant (W m^{-2} K^{-1}), tensile(Pa)

Φ: view factor matrix

ψ: maximum efficiency ratio

Subscripts

0: ambient surface

abs: absorbed

adm: admissible

amb: ambient

C: convection

con: contraction

corr: corrosion

d: duct

D: destruction

deliv: delivered

emi: emitted

exp: expansion

ext: external

field: heliostat field

film: HTF region in contact with the tube internal wall

foul: fouling

g: ground

hel: heliostats

HTF: heat transfer fluid

i: emitting surface

in: inlet

int: internal

j: absorbing surface

k: intermediate reflecting surface

l: intermediate reflecting surface

L: losses

m: mirrors

min: minimum

n+1: rear wall surface

net: net

opt: optical

out: outlet

press: pressure

R: radiation

rec: recalculated

ref: reference

refle: reflected

S: Sun

t: tube

th: thickness

thermal: energy efficiency

tot: whole receiver

wall: tube wall

X: exergy

Abbreviations

CSP: concentrating solar power

ECGM: energy coarse grid model

HTF: heat transfer fluid

LCOE: levelized cost of electricity

SPT: solar power tower

XCGM: exergy coarse grid model

1. Introduction

The solar resource constitutes an excellent alternative to the traditional energy sources, given its abundance on the Earth surface. Hence, in a worldwide landscape increasingly becoming aware of the global warming and the use of fossil fuels negatively impacting the environment [1], it comes as no surprise that its application for electricity production has followed a rising tendency in the last years. The renewable energy share related to the power generation has increased from the 20% in 2010 to the 25% in 2017/2018 [2] and in that same time period, the GWh of electricity production due to the solar energy has experienced a growth of a 870% [3].

Solar radiation on the Earth surface is available every day and it becomes especially interesting for electricity production applications in locations benefiting from a high direct normal irradiance (DNI) [4]. The most favourable regions in such sense are placed in the so-called 'Sun Belt', with not only a great amount of solar radiation available but also a vast quantity of sunshine hours and few cloudy periods. Despite these highly desirable conditions, the solar radiation is not available during the night periods and unpredictable interruptions of the solar radiation may still occur, such as cloud passages. Under these circumstances, in order to be able to uninterruptedly dispatch power, and so diminish the dependence on nuclear and carbon plants, thermal energy storage is crucial.

Concentrating Solar Power (CSP) technologies take advantage of the solar radiation reflected by a series of mirrors into the surface of a receiver device, transferring thermal energy to a heat transfer fluid (HTF) flowing through its interior. This energy will later be transformed in electricity in the power block. The heated HTF can be stored as well, making

these installations the most relevant renewable alternatives for the traditional base-loads plants. Among the different CSP technologies, Solar Power Tower (SPT) plants are likely to take the lead [5] due to the advantages provided by the higher temperatures that they are able to reach, enjoying greater capacity factor, lower energy storage costs and greater steam cycle efficiency.

On the flip side, the SPT installations demand a great capital investment. Out of the different subsystems integrating a SPT plant, the solar field and the receiver are the ones with the greater costs [5]. The yield improvement of these plants would eventually lead to a higher electricity output, accountable of a 25% LCOE reduction potential [6]. Currently, its high LCOE is one of the main reasons this technology is not growing as rapidly as it potentially could [7]. This situation motivates the efforts of trying to increase these facilities performances, especially focusing the attention on the most critical subsystems.

It is worth stressing that for any energy source, the most important aspect consists in determining what is the maximum quantity of energy that can be transformed in useful work. In order to achieve greater efficiencies, it should be concluded what that solar energy is capable of offering in the SPT plant: its real potential and the ways to maximize its exploitation. Hence, the different causes of losses and irreversibilities should be studied to obtain the actual profitability of the energy. For that purpose, the exergy efficiency analysis is key since it indicates the quality of the energy, considering the useless fraction of it due to irreversibility. More precisely, the work production potential of a certain substance can be studied analyzing its exergy, while for a certain process, the exergy conservation equation is the suitable procedure.

In the solar thermal energy field, and more specifically in the receiver subsystem, the main exergy to analyze is the exergy of radiation of the processes involved. The numerous emissions and absorptions that convert radiation energy into heat are irreversible processes, resulting in exergy losses. The exergy depends highly on the temperature of the absorbing surface, increasing when the temperature grows. Hence, it is understandable the low exergy efficiency in solar driven processes and devices [8]: the Sun temperature is around 6000 K and its exergy is degraded to a maximum temperature of 840 K in the HTF outlet, in the case of a solar salt receiver. The exergy efficiency also increases the lower the ambient temperature is, since a substance or process can produce work until it reaches the dead state, which is no other that the thermal equilibrium with the surroundings. Thus, in a SPT plant is not only important the DNI in the location selected, as stated above. There is also room for improvement in the way that solar irradiation is used for the electricity production.

Given its relevance and usefulness in process engineering, some authors have focused their research in understanding the exergy of radiation. Petela paved the way with its work [9], introducing the equations for the calculation of such radiation exergy. He later further developed his previous studies in [10], where he found that there is an optimum temperature for the absorbing surface. A reasonable outcome since a high temperature translates in a higher exergy but it also produces greater energy losses due to the emission of the surface. The results obtained by Petela regarding radiation exergy were reaffirmed in [11]. In a more wider field, second law analysis gained popularity in the analysis of heat transfer processes, introducing the entropy minimization in the design process and highlighting the importance of the study of irreversibility in the thermodynamic

performance of heat transfer devices [12]. The work [13] remarks the relevance of the thermophysical properties of the HTF used in the heat transfer devices regarding the entropy generation minimization.

Different exergy analysis of receivers in CSP technologies have been found in the literature. An experimental exergy analysis of a cylindrical-parabolic cooker was performed by [14], motivating its latter analytical study [8]. The linear Fresnel receiver has also been studied from the exergy viewpoint [15], as well as the parabolic through receiver [16–18]. In [17], the parabolic through receiver is analyzed operating not only with a liquid HTF, Therminol VP1, but also with air, both under various flow rates and inlet temperatures. Other aspects such as the wind velocity or the solar irradiation are examined in [16] for a silicone heat transfer fluid. An in-depth review of the literature available related to the exergy in parabolic collectors is presented in [19]. Regarding the SPT technologies, [20] tested different HTF alternatives performing an exergy analysis of the receiver, proving the great performance of molten salts; however, it did not take into account the circumferential variations of the tubes temperature nor the multiple reflections between surfaces. Not only the receiver subsystem has been studied but also the concentrators [21] of all CSP technologies and the power block [22], including supercritical cycles [23,24]. In the literature, there can be found several global analysis of SPT plants, which have shown that the receiver is among the elements suffering from greater exergy losses [20,22,25] given the high heat fluxes exchanged on that device. However, detailed analysis of the SPT receiver have not been yet conducted.

With everything presented above, the objective of this work is to perform an exergy analysis of the receiver of a SPT plant, coupling its behavior to the heliostat field, since it is the main subject of the radiation heat in such facilities. The principal particularity of this study is that the thermal model that precedes the exergy efficiency calculation has been done for the tubes of the receiver discretized not only in axial divisions, but also in circumferential ones. Hence, the exergy model also considers the temperature gradient in the circumferential coordinate. In this study, the mentioned models are referred to, respectively, as energy coarse grid model (ECGM) and exergy coarse grid model (XCGM). The circumferential cells provide a more precise estimation of the tube wall temperature distribution at its outer surface [26]. As previously discussed, the temperature of the absorbing surface is a highly relevant parameter in the exergy efficiency so this would lead to a more reliable exergetic analysis. Hence, as opposed to the works found in the literature, the tubes are not considered as a single exchange surface for a certain length of the receiver, but rather a series of them, each one at their corresponding temperature. Moreover, the receiver tubes design implemented in the ECGM is such that takes the minimum thickness that is able to endure the pressure and the corrosive effects present during the receiver expected lifespan, aiming to lower the entropy generation.

In the present study, Section 2 describes the discretization of the geometry of the receiver and shows the modelling selected, both for the thermal resolution of the receiver with the ECGM and the exergy balance and efficiency with the XCGM. In Section 3, the chosen design parameters of the SPT plant are indicated: the ambient conditions and the heliostat field and receiver configurations. The results obtained for the case of study are shown in Section 4, as well as the comparison with the ones resulting from the modification of the optical properties of the tubes coating, the aiming strategy of the heliostat field, the DNI and

the ambient temperature. Finally, the main conclusions reached with this analysis are summarized in Section 5.

2. Proposed modelling

SPTs are constituted by three main subsystems well differentiated from one another, namely: the heliostat field, the receiver and the power block. The heliostat field consists in a series of mirrors, provided with sun-tracking systems, that reflect and concentrate direct solar radiation into the receiver surface. The latter may appear in different configurations but all of them have the same objective: to heat the HTF until a maximum allowable temperature, that may be dictated by the HTF itself or by the constructive properties of the receiver. Lastly, the thermal energy carried with the HTF is transformed into electricity in the power block.

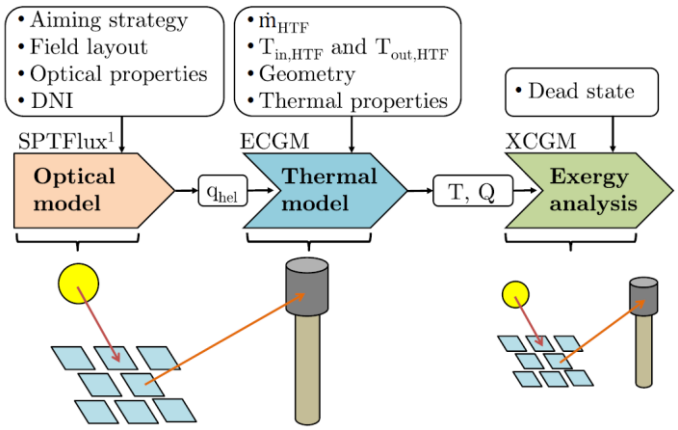

Figure 1. Models involved in the receiver exergy analysis.

In order to analyse the receiver, the discretization of its characteristic geometries needs to be described, which is done in Section 2.1. Also, although the present study is only focused on the receiver subsystem, the interaction with the upstream elements and their influence cannot be neglected if the purpose is to realistically analyse the behaviour of the receiver as a part of a SPT plant. Hence, the configuration and behaviour of the heliostat field is especially relevant for such study, since it dictates how the heat flux is distributed on the receiver surface. In this case, the software tool SPTflux[1] [27] has been used for that end, serving as the optical model and providing the information needed to couple the heliostat field operation to the receiver. Using that knowledge and data, the thermal model of the receiver is separately developed, as presented in Section 2.2. With it, the receiver is fully characterized in terms of energy exchanged between surfaces and transferred to the HTF during its steady state operation. The temperatures of the diverse surfaces interfering are also obtained. Thereafter, the exergy analysis of the receiver can be fully undertaken following the procedure in Section 2.3. The interaction between the different models and modules used for the exergy analysis of the receiver is shown in Figure 1.

2.1. Discretization of the receiver

The system studied is an external tubular receiver, which is now introduced in a simplified way. Its particularities will be further detailed in Section 3, where the selected

[1] http://ise.uc3m.es/research/solar-energy/fluxspt/

case of study is presented. The receiver has at its core a cylindrical shape that will be referred to as base cylinder or rear wall indistinctly. This base cylinder reflects greater amount of insolation and serves of frame to support a series of vertical panels that are constituted by the tubes conducting the HTF. The panels are also composed by an inlet and outlet collector that, respectively, distribute equally the HTF mass flow in all the tubes and regroup it.

To obtain the exergy generated in the receiver subsystem, the different agents interacting need to be properly delimited: the receiver tubes, the base cylinder and the ambient, as schematically depicted in Figure 2.a for two consecutive tubes of a panel.

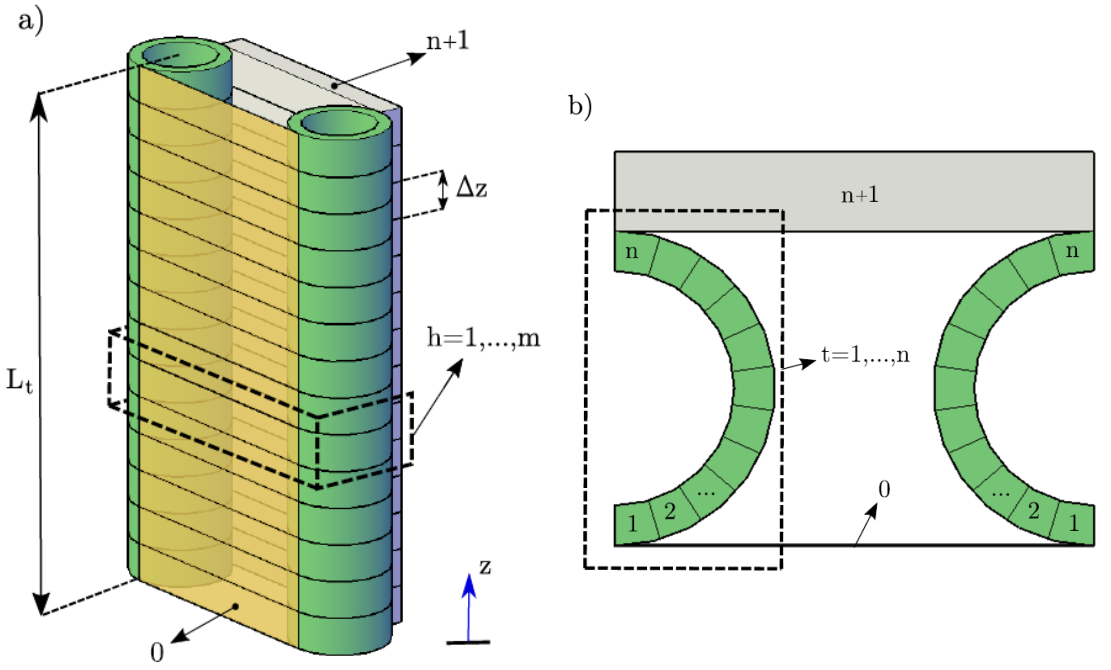

Figure 2. a) Discretization of the geometries interacting in an external receiver b) Plant view of one axial division.

The tubes, whose length is named as L_t (m), from all the panels are all equally divided in a series of axial and circumferential divisions. The axial divisions encountered by the HTF through its whole path, from the receiver inlet to the receiver outlet, are counted with the index *h*, that goes from 1 to *m,* being *m* the total number of axial divisions. These axial parcels present a height of $\triangle z$, which is selected long enough to allow the assumption of the hypothesis of a bidimensional radiative heat exchange. Thus, the interaction between axial divisions at different "levels" from one tube to the other does not occur. It does not mean that just a single set of axial division out of the whole receiver is studied, but that they must be analysed separately depending on their *z* position. Hence, the study focuses on the exchanges in one certain axial *division level*, *h*, at a time. This makes the circumferential cells of the tubes the relevant ones for the energy exchanges between surfaces at an axial position. The circumferential divisions in a specific axial level *h* of one tube are collectively referred to as *t* and go from 1 to *n*. The rear wall has been considered to be touching the rear side of the tubes, as represented in Figure 2.b. Hence, for the radiative exchange, adjacent tubes can be reduced to two tube halves facing, since they are confined between the rear wall and the imaginary surface representing the ambient. This is not the case in real life

receivers, where there is a gap between the base cylinder and the tubes. Such simplification has been adopted to ease the view factors calculation. It is a reasonable assumption justified by the small distances between adjacent tubes and between the tubes and the base cylinder. Thus, given the symmetry of the present scenario, *n* is the total number of parcels in half the cross section of a tube.

On the other hand, the rear wall is a portion of the base cylinder extending between the two tubes halves limits. It is designated with the *n+1* subscript and it is also discretized in the same number of axial cells than the tubes. Therefore, each set of half tubes divisions has a corresponding *h* rear wall portion with a uniform temperature, T_{n+1}, along its surface but differing from one axial division to another.

The emission of the tubes and the rear wall at a *h* level can be written as

$$E_i = A_i \varepsilon_i \sigma {T_i}^4, \quad i = 1, 2, \dots, n+1, \tag{1}$$

where A_i is the area of the different surfaces (m^2), ε_i is the emissivity, σ refers to the Stefan-Boltzmann constant (5.67×10^{-8} W m^{-2} K^{-1}) and T_i corresponds to the temperature of each cell (K).

Lastly, the surface *0* is an imaginary surface that represents the ambient around the receiver, which supplies in a diffuse way the direct insolation reflected by the heliostat field. The surroundings find themselves at the following temperature [28] in all of the *h* divisions

$$T_0 = T_{ref} = \frac{\left[\left(\varepsilon_{amb} T_g\right)^4 + \left(\varepsilon_g T_{amb}\right)^4\right]^{1/4}}{\left[\varepsilon_{amb} + \varepsilon_g\right]^{1/4}}. \tag{2}$$

Here ε_{amb} and ε_g represent the ambient and ground emissivity respectively. ε_{amb} depends on the ambient pressure, the temperature at the location of the receiver, T_{amb}, the relative humidity and the solar time. T_g is the ground temperature. This T_0=T_{ref} temperature is taken into account for the thermal analysis of the receiver and as the temperature of the dead state. However, the temperature at which surface *0* emits is regarded to be the temperature of the Sun surface, $T_0 = T_S$, 6000 K, as considered by Petela [8]. At an *h* level, the emission of the surroundings surface is

$$E_0 = A_0 q_{hel}, \tag{3}$$

where A_0 is the area of such surface and q_{hel} is the heat flux arriving from the heliostat field (W m^{-2}). It is not a uniform heat flux as a whole; just like the rear wall, it is divided in a series of *h* cells in which the heat flux is uniform, but different from one division to the other, as it will be depicted in Section 4.

2.2 Thermal model of the receiver (ECGM)

The radiative exchanges between neighbouring tubes are analysed for just two facing halves, as discussed in Section 2.1. Also, the present model contemplates not only axial divisions of the tubes but circumferential partitions as well, which lead to a more accurate

calculation of the radiation losses, increasing the precision of the tube temperatures obtained [26].

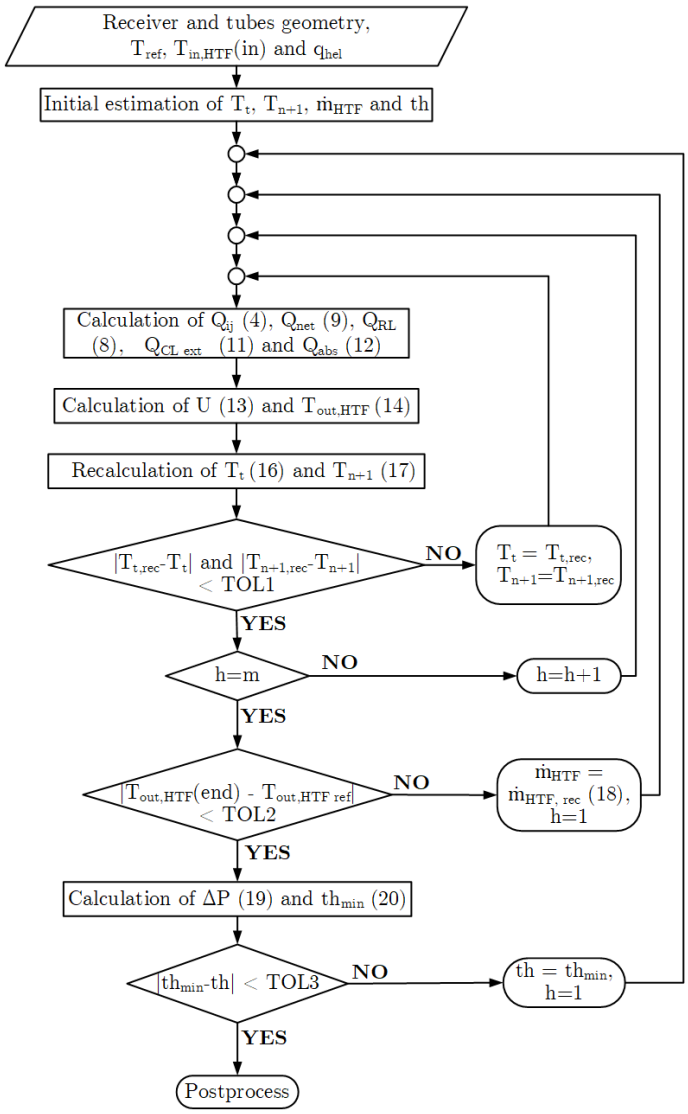

Figure 3. Iterative process of the thermal model.

The initial parameters are the geometrical characteristics of the receiver and the tubes, the inlet temperature of the HTF, $T_{in,HTF}$, and the desired outlet one, $T_{out,HTF\ ref}$, as well as the heat flux on the receiver surface arriving from the heliostat field at every *h*, q_{hel}. Although the thickness of the tubes, *th*, is assumed at the beginning alongside the rest of the geometrical parameters, the model is designed so it is recalculated. The objective of the recalculation is to finally set the thickness in the minimum value allowable to meet the safety requirements, aiming to decrease the entropy generation of the receiver. The temperature of the tube and rear wall surfaces, T_t and T_{n+1}, as well as the HTF mass flow, $\dot{m}_{HTF}$, are also initially presupposed, although they are recalculated, $T_{t,rec}$, $T_{n+1,rec}$ and $\dot{m}_{HTF,rec}$, until the HTF leaves at the desired outlet temperature.

The calculation process, illustrated in Figure 3, is performed as follows:

- In a certain axial division, h, the heat delivered to any surface j by any surface i, Q_{ij}, is obtained considering the emission of surface i, calculated with Eqs. (1) and (3). On the one hand, that heat is constituted by emission leaving from i, E_i, and being absorbed by j with no intermediate reflections. On the other hand, there is the emission arriving from i, E_i, to the absorbing surface j after a succession of reflections involving the rest of the surfaces (k, l…) that are also included in the system. Such reflections occur in between the "departure" of the radiation from i and the "arrival" to j. Hence, the heat Q_{ij} is obtained as

$$Q_{ij} = E_i F_{ij} \alpha_j + E_i \sum_{k=0}^{n+1} F_{ik} \rho_k F_{kj} \alpha_j + E_i \sum_{k,l=0}^{n+1} F_{ik} \rho_k F_{kl} \rho_l F_{lj} \alpha_j + \cdots, \tag{4}$$

where F_{ij} is the view factor between the surfaces involved in the radiative exchange, α_j is the absorptivity of the surface receiving the heat from i, and ρ is the reflectivity of the intermediate surfaces reflecting the emission leaving i. The summation terms regarding the multiple reflections are added in an iterative process until Q_{ij} converges. This set of equations for the delivered heat can be written in matrix form as

$$Q_{deliv} = \begin{pmatrix} Q_{00} & \cdots & Q_{0,n+1} \\ \vdots & \ddots & \vdots \\ Q_{n+1,0} & \cdots & Q_{n+1,n+1} \end{pmatrix} = E\Phi A + E\Phi R\Phi A + E\Phi R\Phi R\Phi A + \cdots, \tag{5}$$

with E, R and A being diagonal matrices for the emission, reflectivity and absorptivity of the surfaces and Φ being the view factors matrix:

$$E = \begin{pmatrix} E_0 & & 0 \\ & \ddots & \\ 0 & & E_{n+1} \end{pmatrix}, \qquad R = \begin{pmatrix} \rho_0 & & 0 \\ & \ddots & \\ 0 & & \rho_{n+1} \end{pmatrix},$$
$$A = \begin{pmatrix} \alpha_0 & & 0 \\ & \ddots & \\ 0 & & \alpha_{n+1} \end{pmatrix}, \qquad \Phi = \begin{pmatrix} F_{00} & \cdots & F_{0,n+1} \\ \vdots & \ddots & \vdots \\ F_{n+1,0} & \cdots & F_{n+1,n+1} \end{pmatrix}. \tag{6}$$

The optical properties for the heat leaving the ambient, *i=0*, are all (surface *i*, surface *j* and intermediate surfaces k, l…) in the visible spectrum, while the properties for the heat leaving the rest of the surfaces *i=1, 2,..., n+1* are the ones in the infrared spectrum. Hence, the matrixes E, A and R presented above have two variants, one for the visible spectrum properties and one for the infrared spectrum properties. This means that the heat delivered matrix, Q_{deliv}, is also obtained for these two cases. The definitive Q_{deliv} is composed by the row corresponding to *i=0* in the visible spectrum Q_{deliv} matrix, and the rows from *i=1* to *i=n+1* from the infrared spectrum one.

With all of the above, the total heat arriving to a tube division j and the rear wall can be expressed as

$$Q_{deliv,j} = \sum_{i=0}^{n+1} Q_{ij}\,, \;\; j = 1, 2, \dots, n+1, \tag{7}$$

while the radiation losses can be understood as the heat delivered to the ambient,

$$Q_{RL} = Q_{deliv,0} = \sum_{i=0}^{n+1} Q_{i0}\,. \tag{8}$$

- Hence, the net heat intercepted by the *j* surface, prior the external convection losses, is the difference between the heat extracted from it and the heat delivered to it that it absorbs.

$$Q_{net,j} = E_j - Q_{deliv,j}. \tag{9}$$

A negative net heat means that the surface absorbs energy indeed, while a positive one indicated that it delivers heat to the system. The addition of all the net heats involved in the system must be zero,

$$\sum_{j=0}^{n+1} Q_{net,j} = Q_{net,0} + Q_{net,t} + Q_{net,n+1} = 0, \tag{10}$$

where $Q_{net,t} = \sum_{j=1}^{n} Q_{net,j}$. However, the heats will be treated in terms of their absolute value for the following calculations.

- The external convection losses, $Q_{CL\,ext}$ are obtained as

$$Q_{CL\,ext,j} = h_{ext,j} A_j \left(T_j - T_{ref}\right), \;\; j = 1, 2, \dots, n, \tag{11}$$

where A_j is the area (m^2) of surface *j* and h_{ext} is the external convective coefficient ($Wm^{-2}K^{-1}$), obtained for cylindrical external receivers as presented by [29] taking into account both natural and forced convection.

- Once Q_{net} and $Q_{CL\,ext}$ are known, the heat absorbed by the tubes can be calculated

$$Q_{abs,j} = Q_{net,j} - Q_{CL\,ext,j}, \;\; j = 1, 2, \dots, n. \tag{12}$$

- It is considered the turbulent and fully developed regime flow of the HTF so the Petukov correlation is used to obtain the Darcy factor [30]. That factor is used in the Gnielinski correlation [31] to calculate the Nusselt number for the internal convective coefficient, h_{int}. Then, the global transfer coefficient is obtained as

$$U = \left(\frac{1}{h_{int}} \frac{d_{ext}}{d_{int}} + \frac{d_{ext} \ln(d_{ext}/d_{int})}{2k_t} + R_{foul} \frac{d_{ext}}{d_{int}} \right)^{-1} \tag{13}$$

taking into account the convection inside the tube, the effect of the thermal conductivity of the tube wall with k_t ($W\,m^{-1}\,K^{-1}$) and the fouling inside the duct with the resistance R_{foul} ($m^2\,K\,W^{-1}$). The d_{ext} and d_{int} (m) are the external and internal diameters of the tube, respectively.

Given that for the first axial division, the inlet temperature of the HTF, $T_{in,HTF}$, is known, the outlet temperature of the HTF is calculated as

$$T_{out,HTF} = \overline{T_t} - \left(\overline{T_t} - T_{in,HTF}\right) exp\left(\frac{U\ p\ \Delta z}{\dot{m}_t\ Cp}\right), \tag{14}$$

where p is the tube perimeter (m), Cp is the heat capacity of the HTF (J kg^{-1} K^{-1}), $\dot{m}_t$ is the HTF mass flow inside one tube (kg s^{-1}) and $\overline{T_t}$ is the mean temperature in the tube surface (K):

$$\bar{T}_t = 2\ \frac{\sum_{j=1}^{n} A_j\ T_j}{p\ \Delta z}. \tag{15}$$

- The temperature of the tube is recalculated, since it was estimated at the beginning of the process:

$$T_{j,rec} = \frac{Q_{abs,j}}{A_j U} + \frac{T_{out,HTF} + T_{in,HTF}}{2}, j = 1, 2, \dots, n. \tag{16}$$

Regarding the rear wall, it is considered to be reradiating, which means that it is an adiabatic surface where the heat absorbed is equal to the heat leaving from it. Thus, the net heat at surface *n+1* must be zero. This allows us to recalculate the temperature at the rear wall as

$$T_{n+1,rec} = \left(\frac{Q_{deliv,n+1}}{A_{n+1}\varepsilon_{n+1}\sigma}\right)^{1/4}. \tag{17}$$

- Since the temperatures of the tube and rear wall were initially estimated, the recalculated temperatures are checked with the previous ones. The steps above are repeated until the temperatures of the precedent iteration are within the selected tolerance range with respect to the recalculated ones.

- As for the following axial cell, its $T_{in,HTF}$ is the same that the $T_{out,HTF}$ of the previous division, and so on. The $T_{out,HTF}$ of the final cell of the last panel must match the desired outlet HTF temperature, $T_{out,HTF\ ref}$. Thus, the outlet temperature of the salts at the end of the receiver needs to be checked. If it is not the one expected, a new mass flow of the HTF is recalculated, and the previous procedure is performed again until the convergence is reached. The new mass flow is established to be

$$\dot{m}_{HTF,rec} = \dot{m}_{HTF} + \dot{m}_{HTF}\left[\bar{T}_{out,HTF}(end) - \bar{T}_{out,HTF\ ref}\right]. \tag{18}$$

- In the next step, the total pressure drop, ΔP (Pa) in the receiver is obtained. Not only the straight tube sections are taken into account, but also the elbows, straight connectors and manifolds need to be included as a relevant part of the pressure losses [32],

$$\Delta P = \sum_{straight} f_r \frac{L_d \dot{m}^2}{2 d_d \rho C^2} + \sum_{exp/con} K \frac{\dot{m}^2}{2\rho C^2} + \sum_{elbow} \left[\left(1.3 - 0.29\, ln\left(\frac{Re}{10^5}\right) \times 0.21 a_1 \left(\frac{R_0}{d_d}\right)^{-\frac{1}{4}} \right) \right] \frac{\dot{m}^2}{2\rho C^2}, \quad (19)$$

where *fr* is the Darcy friction factor, L_d is the length of the straight duct (m), d_d is its internal diameter (m), $\dot{m}$ the HTF mass flow through that duct (kg s^{-1}) and ρ is the HTF density (kg m^{-3}). *Re* is the Reynolds number, *C* is the cross-section area of the tubes (m^2), R_0 is the elbow curvature radius (m) of the pipe, a_1 is a coefficient depending on the angle covered by the elbow and *K* is the resistance coefficient for expansions and contractions happening at the inlet and outlet of the manifolds: $K_{exp} = \left(1 - {}^{C_1}/_{C_2}\right)^2$ and $K_{con} = 0.5\left(1 - {}^{C_2}/_{C_1}\right)$ [32].

- Knowing the pressure drop, the minimum allowable thickness can be obtained. It must be such that the tubes are able to endure the working pressure at their inside as well as the corrosive effects of the HTF flowing through them during the whole operative life of the receiver. The term related to the corrosion, th_{corr}, is obtained as the corrosion ratio, *cr*, by the expected lifecycle of the plant, *lc*. As for the pressure term, th_{press}, the minimum thickness is calculated as presented in section 8 of the ASME code for Boiler and Pressure Vessel [33],

$$th_{min} = th_{corr} + th_{press} = cr \cdot lc + \frac{\Delta P\, d_{int}}{2(\sigma_{adm} E_1 - 0.6\Delta P)} = cr \cdot lc\, \frac{\sigma_{adm} E_1 - 0.6\Delta P}{\sigma_{adm} E_1 + 0.4\Delta P} + \frac{\Delta P d_{ext}}{2(\sigma_{adm} E_1 + 0.4\Delta P)}. \quad (20)$$

Here σ_{adm} (Pa) is the maximum admissible tensile, evaluated at the tube working temperature and E_1 is the joint efficiency factor coefficient, that takes the value 1 for seamless tubes. While the second part of the equation is originally presented in terms of the internal diameter, the global expression has been recalculated to write it related to the external one. This is so to avoid the modification of the external diameter with the new thickness when working with the internal diameter expression, which would lead to a possible number of tubes per panel alteration, complicating the iterative process. If that minimum thickness calculated does not correspond to the one initially selected, the whole process is done over from the beginning, taking this minimum thickness as the new value for the next iteration.

2.3 Exergy calculation (XCGM)

In a SPT central receiver, the energy conversion from solar irradiation to heat is a radiation driven process. Thus, relying on radiation heat, optical properties and geometry pay an important role.

To study the exergy in such receiver, the different energy exchanges, from the Sun irradiating to the heat transfer to the HTF, need to be included in the analysis. With that in mind, the maximum efficiency ratio [9] must be obtained in the first place for each emitting surface at each axial division as

$$\psi_i = 1 + \frac{1}{3}\left(\frac{T_{ref}}{T_i}\right)^4 - \frac{4}{3}\frac{T_{ref}}{T_i}, \quad i = 0, 1, \dots, n+1, \tag{21}$$

where, as stated in Section 2.1, T_0 is the Sun temperature in the exergy analysis. Therefore, $\psi_0 = \psi_S$. This exergy efficiency ratio is a characteristic parameter involved in radiation processes and is obtained as the quotient between the maximum work that can be obtained from radiation energy and the energy of such radiation.

Then, the processes involved in the SPT external receiver are analysed with the expression for the exergy conservation. For a single axial division the balance is written as

$$X_S = X_{opt} + X_0 + X_t + X_{n+1} + X_{CL\,ext,t} + X_{wall,t} + X_{D,HTF} + X_{HTF} \tag{22}$$

On the one hand there is the solar exergy inlet of the system, that must be equal to the different radiating fluxes, the exergy losses and destructions due to irreversible processes in the receiver and the net exergy finally exiting the receiver in the HTF, which is the difference between the exergy outlet and inlet of the HTF, $X_{HTF} = X_{out} - X_{in}$. The exergies appearing in an axial discretization are depicted in Figure 4.

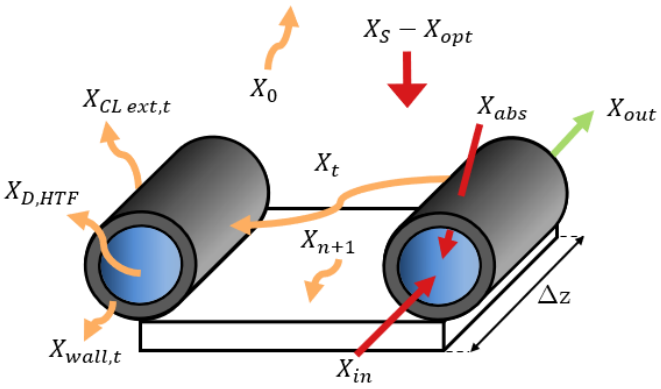

Figure 4. Exergies schematic representation.

The different terms in the balance are:

- The exergy of the sunlight incident in the heliostat field,

$$X_{S,tot} = \psi_S\, DNI\, A_m. \tag{23}$$

Being the *DNI* the direct normal irradiation (W m^{-2}) and A_m the total mirrors area in the heliostat field. It represents the exergy initially entering the system. The subscript *tot* means that the exergy is referred to the whole receiver, not just one axial division.

Some of that sunlight exergy is lost in the reflection and concentration of the direct irradiation from the mirrors to the receiver surface. This is the exergy loss in the heliostat field,

$$X_{opt,tot} = \psi_S\, DNI\, A_m \left(1 - \eta_{field}\right), \tag{24}$$

where η_{field} is the average optical efficiency of the heliostat field.

For an axial division, the difference between X_S and X_{opt} results in the exergy arriving to the receiver through surface *0* at a certain *h.* Hence, it is the emission E_0 of that surface multiplied by the exergy efficiency ratio at Sun temperature:

$$X_S - X_{opt} = \psi_S E_0 = \psi_S \, q_{hel} \, A_0. \tag{25}$$

- Part of the exergy escapes from the receiver system through surface *0* because of the reflections of the heat emitted by surfaces *0, 1,..., n+1*,

$$X_0 = \sum_{i=0}^{n+1} \psi_i \, Q_{i0}. \tag{26}$$

This irreversible exergy loss can be divided into the fraction that escapes the system, which originally came from surface 0 and has not been absorbed by the tubes (just a reflection process), $X_{0,\,refle}$, and the fraction that comes from the emission of the tubes and the rear wall and, after at least one reflection in the adjacent tube or in the rear wall reaches *0*, $X_{0,\,emi}$.

- There are also exergy losses due to the multiple irreversible emissions and absorptions in the tubes. These losses exist because, although the heat is eventually absorbed by the tubes, the availability of such heat is dictated by its temperature, which can differ from the temperature of the emitting surface. Therefore, such exergy destruction in *j* is obtained as the difference between the exergy gains minus the exergy losses. Regarding the gains, these are the heats arriving from surfaces *i* at temperature T_i ($\psi_i Q_{ij}$) and the heat needed for emission of surface *j* ($\left(1 - T_{ref}/T_j\right)E_j$). On the other hand, the exergy outlets are the emission of surface *j* at T_j ($\left(1 - T_{ref}/T_j\right)Q_{ij}$) and the heat from surface *i* absorbed as heat by *j* at temperature T_j ($\psi_j E_j$):

$$X_t = \sum_{j=1}^{n} X_j = \\ = \sum_{j=1}^{n}\left(1 - \frac{T_{ref}}{T_j} - \psi_j\right)E_j + \sum_{j=1}^{n}\sum_{i=0}^{n+1} \psi_i Q_{ij} - \sum_{j=1}^{n}\sum_{i=0}^{n+1}\left(1 - \frac{T_{ref}}{T_j}\right)Q_{ij}. \tag{27}$$

- The same irreversible exergy losses are present at the rear wall. Thus, in this case, *j* is just surface *n+1*

$$X_{n+1} = \left(1 - \frac{T_{ref}}{T_{n+1}} - \psi_{n+1}\right)E_{n+1} + \sum_{i=0}^{n+1} \psi_i Q_{i\,n+1} - \sum_{i=0}^{n+1}\left(1 - \frac{T_{ref}}{T_{n+1}}\right)Q_{i\,n+1}. \tag{28}$$

- Exergy destruction due to irreversibility of the external heat convection in the *j* surfaces of the tube wall,

$$X_{CL\,ext.t} = \sum_{j=1}^{n} Q_{CL\,ext,j}\left(1 - \frac{T_{ref}}{T_j}\right). \tag{29}$$

- Exergy flow in the tube wall, which deals with the heat conduction through it,

$$\begin{aligned} X_{wall,t} &= \sum_{j=1}^{n} Q_{abs,j}\left(\frac{T_{ref}}{T_{film}} - \frac{T_{ref}}{T_j}\right) = T_{ref}\Delta S_{th} \\ &= T_{ref}\int_{z=0}^{\Delta z}\int_{0}^{2\pi} \frac{k_t}{\ln\left(1+\frac{th}{d_{int}/2}\right)} \frac{\left(T_j - T_{film}\right)^2}{T_j\, Tfilm}\, d\theta\, dz, \end{aligned} \tag{30}$$

with T_{film} (K) being the salt temperature in contact with the tube internal wall at *j=1, 2,…, n*.

- Exergy destruction occurring in the HTF, considering the fouling resistance and the internal convection when transferring the heat to the HTF from the inner tube wall and the friction of the HTF with the tube walls [34]:

$$\begin{aligned} X_{D,HTF} &= T_{ref}\Delta S_{gen} = T_{ref}(\Delta S_{gen,\Delta T} + \Delta S_{gen,\Delta P}) \\ &= T_{ref}\left[\int_{z=0}^{\Delta z}\int_{0}^{2\pi} \frac{0.5 d_{int}\left(T_{film} - T_{HTF}\right)^2}{\left(\frac{1}{h_{int}}\frac{d_{ext}}{d_{int}} + R_{foul}\frac{d_{ext}}{d_{int}}\right) T_{HTF} T_{film}}\, d\theta\, dz + \frac{\dot{m}_t \Delta P}{T_{HTF}\rho}\right]. \end{aligned} \tag{31}$$

- The last term in the balance is the net exergy gain in the HTF

$$X_{HTF} = X_{out} - X_{in} = \sum_{j=1}^{n}\left[Q_{abs,j}\left(1 - \frac{T_{ref}}{T_{film}}\right)\right] - T_{ref}\Delta S_{gen}\,. \tag{32}$$

Finally, the exergy efficiency of that *h* axial division of the SPT receiver is calculated as the exergy of the process output, leaving the HTF, over the exergy of the input from the Sun:

$$\eta_X = 100\,\frac{X_{HTF}}{X_S}. \tag{33}$$

The percentages of the exergy destruction and losses involved in the balance ($\xi_{X_{opt}}$, ξ_{X_0}, ξ_{X_t}, $\xi_{X_{n+1}}$, $\xi_{X_{CL\,ext,t}}$, $\xi_{X_{wall,t}}$, $\xi_{X_{D,HTF}}$) can be obtained in the same way in order to analyse how much they contribute in the exergy destruction in the system. They can also serve to determine where there is still room for improvement in the receiver design, coupled with the heliostat field performance. Thus, Eq. 22 can be rewritten in terms of the exergy efficiency and losses as:

$$100 = \xi_{X_{opt}} + \xi_{X_0} + \xi_{X_t} + \xi_{X_{n+1}} + \xi_{X_{CL\,ext,t}} + \xi_{X_{wall,t}} + \xi_{X_{D,HTF}} + \eta_X\,. \tag{34}$$

On the other hand, the thermal efficiency of the receiver and heliostat field can be obtained as:

$$\eta_{thermal} = 100 \frac{Q_{abs}}{Q_{hel}} \eta_{field} \,. \tag{35}$$

3. Case of study

In the previous sections, the procedure to analyse the exergy of a tubular external receiver has been introduced. It has been done trying to include the least possible particularities, aiming to provide a generalized method for the study of this specific subsystem. Now, the parameters of the selected receiver configuration are presented.

3.1 Ambient conditions

Regarding the conditions of the surroundings of the SPT plant, the ones selected are an ambient pressure of 1 atm, an ambient temperature, T_{amb}, of 25 °C and a relative humidity of 60%. With such conditions, ε_{amb} results in 0.8506. The ground emissivity is 0.955 and its temperature is obtained as $T_{amb}\ \varepsilon_S^{1/4}$ [28]. The wind velocity is null so the external convection is due only to the natural convection effect. The latitude of the location is 37.56°.

The ambient conditions are important in the exergy analysis since the maximum work depends on them because the ambient temperature defines the dead state.

3.2 Heliostat field

The heliostat field chosen in the software tool SPTFlux is a Gemasolar-like one, with 2650 heliostats of 115.7 m² of mirror each. This makes a total mirror surface, A_m, of 306605 m².

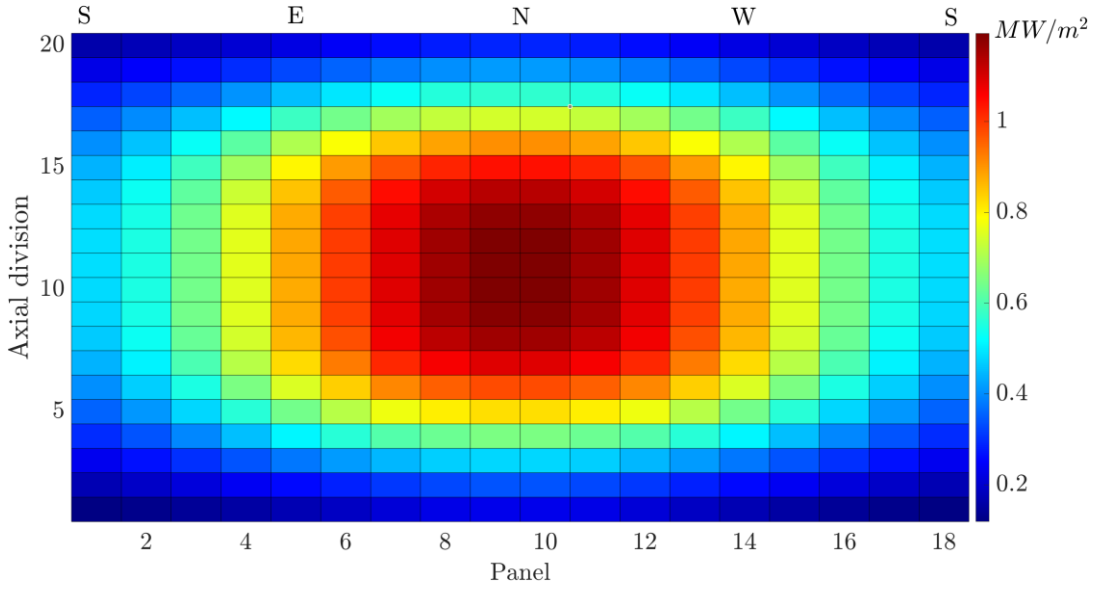

Figure 5. Discretized heat flux distribution on the receiver surface with the flat aiming strategy.

The design point is the solar-noon spring equinox, when the DNI incident on the mirrors is 930 W m^{-2}, and the aiming strategy is a flat one, making the heat flux incident on the receiver as axially homogeneous as possible on its surface, minimizing the peak fluxes

which are harmful to the receiver [27]. Selecting that aiming strategy, the mean optical efficiency of the field, η_{field}, obtained is 58.59%.

The chosen aiming strategy and the mirrors field characteristics result in the heat flux on the receiver surface shown in Figure 5. Such heat flux has been discretized in a series of vertical and horizontal divisions. Since the radiation received by all the tubes of a panel is considered to be the same, these divisions have been done in such way that the number of vertical discretizations is equal to the number of axial divisions of one tube while the horizontal ones correspond to the number of panels. For each individual cell, the heat flux is considered homogeneous.

3.3 Receiver configuration

The receiver is an external tubular receiver placed at the top of a 130 m high tower. The base cylinder of the receiver has a diameter, D, of 8.4 m and serves of supporting frame for 18 equal panels, N_p, that hold the tubes vertically disposed. The external tube diameter has been set to 4.22 cm. The separation between the tubes of a panel is 4.1 mm. That diameter and tube gap result in 32 tubes per panel. The initial thickness of the tube wall has been set in 1.65 mm. However, as stated in Section 2.2, it is later recalculated so the entropy generation due to the heat conduction through the wall is minimized. The length of the tubes, L_t, is 10 m.

Solar salt (60% KNO_3, 40% $NaNO_3$) is selected as the HTF in this receiver, as in the case of the commercial SPT plants [35,36]. The inlet temperature, $T_{in,HTF}$, is 290 °C to avoid its freezing, while the outlet temperature, $T_{out,HTF}$, is limited at 565 °C, preventing its decomposition [37]. The salt mass flow after the iterative process of the thermal model results in 358.76 kg s^{-1} since the receiver is expected to produce 150 MWt. The salt properties can be obtained in [37]. A two path flows configuration, symmetrical in the N-S direction, has been selected [38]. The inlet of the salt is at the bottom of the two northern panels while the outlet is at the top of the most southern ones. Since the crossover between patterns has been shown irrelevant at the solar noon [38], no crossover has been implemented. The total HTF mass flow is equally divided into all the tubes of a panel, and hence the HTF mass flow in one tube results

$$\dot{m}_t = \frac{\dot{m}_{HTF}}{N_{fp}\, N_t}, \tag{36}$$

being N_{fp} the number of path flows for the HTF through the receiver and N_t the number of tubes per panel.

The material selected for the tubes manufacturing is Inconel 625, a highly available material which has been widely studied in the present field. Its properties are available in [33]. The tubes are guided through the panel by a series of equally spaced supports along its length, called clips. These prevent the tubes from bowing excessively, both in the radial direction of the receiver and towards the adjacent tubes of the panel. Three smoothly bended pipes connect the tubes to their respective inlet and outlet collectors, with two elbows of 120° and one of 60°. This results in a_1 coefficients in Eq. (21) of 1.16 and 0.78 respectively. The curvature radius of the elbows, R_0, is 0.13 m. Also, the HTF inside the

collectors is considered to experience a trajectory similar to the circulation inside two 90° elbows, with an a_1 coefficient of 1. There are two 90° elbows in the section connecting two consecutive panels as well. For the pressure drop calculation in the receiver, only the elements in series, not in parallel, are considered; this means that only one flow path is studied, as well as just one tube per panel in that flow path. In Eq. (21), the length of the straight ducts, L_d, the internal diameter of such ducts, d_d, and the mass flow of HTF through them, $\dot{m}$, are:

- For the receiver tubes, L_t, d_{int}, and $\dot{m}_t$.
- For the straight sections after the elbows connecting the tubes to the collectors, lengths of 0.7 m, 1.7 m and 0.2 m per tube, d_{int}, and $\dot{m}_t$.
- For the manifolds, the width of the panel or the length of the collector, 1.4811 m, the internal diameter of the collector 162.76 mm, and the total mass flow through one flow path, $\dot{m}_{HTF}/N_{fp}$.
- For the ducts connecting the inlet and outlet manifolds from different panels, lengths of 0.25 m and 0.599 m (half the length of the whole pipe), 170 mm of d_d, and $\dot{m}_{HTF}/N_{fp}$.

The mentioned connecting sections are presented in Figure 6. The only ones that are insulated are the receiver tubes, being the remaining three different kind of components at a constant temperature. The considered fouling resistance inside the tubes is 8.8×10^{-5} (K m^2 W^{-1}). The corrosion ratio of the Inconel 625, with solar salt flowing through and at a film temperature of 600 °C, is 16.8×10^{-6} (m year^{-1}) [39], while the expected lifecycle of the plant has been set to 30 years.

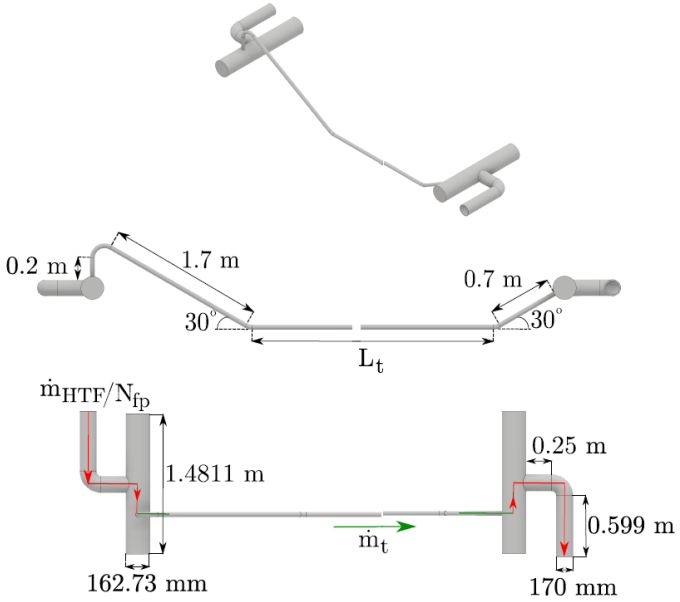

Figure 6. Schematic of the elements considered for the pressure drop calculation in one panel. Only one tube has been depicted.

All tubes are covered with a black Pyromark coating in order to increase their absorptivity. On the other hand, the base cylinder (surface *n+1*) is covered with a white Pyromark ceramic painting of high reflectivity. The optical properties of both coatings when applied on Inconel 625 are presented in Table 1 for both the visible and infrared spectrum.

The properties considered for surface *0* have also been included. The imaginary ambient surface in reality presents a transmissivity of 1, since all the radiation that it receives passes through it without increasing its temperature, making the absorptivity and reflectivity 0. However, for the ECGM and XCGM, this imaginary surface has been modelled like an opaque surface with an absorptivity of 1 (thus reflectivity and transmissivity are 0) and leaving its temperature fixed as T_{ref}, resulting in the same outcome.

Table 1. Optical properties considered.

		Visible spectrum		**Infrared spectrum**		
Coating	**Surface**	**α**	**ρ**	**α**	**ρ**	**ε**
-	**Ambient (*0*)**	1	0	1	0	1
Black Pyromark	**Tube (*1,..., n*)**	0.93 [37]	0.07	0.95 [40]	0.05	*f(T)*, from 0.81 for 588 K to 0.94 for 1366 K [41]
White Pryomark	**Rear wall (*n+1*)**	0.2	0.8 [37]	0.215	0.785 [42]	0.84 [37]

Regarding the thermal model, it is used to study the whole receiver by analysing just one representative tube per panel. This simplification is feasible since the heat flux reaching the tubes surface is considered to be the same in all of them, leading them to have the identical temperature distribution. However, the radiative influence of the adjacent tubes of the panel is indeed taken into account. The insolated straight zone of the tubes is discretized in a series of 74 circumferential cells (n=37) and the axial divisions are 0.5 m long (Δz), giving a total of 20 of them per tube. Therefore, following one flow path (9 panels) and studying just one tube per panel, the number of axial divisions faced is m=180,

$$m = \frac{L_t\, N_p}{\Delta z\, N_{fp}}. \tag{37}$$

The tolerance values selected for the iterative process are: 10^{-3} (K) for TOL1, 10^{-3} (K) for TOL2 and 10^{-6} (m) for TOL3, see Figure 3. TOL1 is the condition for the convergence of the tube and rear wall temperature, TOL2 is the one for the convergence of $T_{out,HTF}$ and TOL3 the one for the convergence of the thickness of the tubes.

4. Results

The exergy analysis has been performed for the receiver for the case of study introduced in Section 3. To do so, the different exergies conforming the balance in Eq. 22 have been obtained. It has been done for all of the axial levels of the panels corresponding to one of the two flow paths in which the receiver has been discretized. Given the symmetry of the heat flux on the receiver surface at solar noon, the exergy results are the same for the remaining flow path. Hence, the total amount of the different exergies is obtained as the sum of the exergies of the 180 axial divisions of one flow path and multiplying that sum by the

number of tubes per panel and flow paths. The Sankey diagram for the case of study is presented in Figure 7.

The exergy efficiency of the configuration chosen is a 32.05%. The results show that the maximum exergy loss occurs in the heliostat field, X_{opt}, being almost half of the exergy that arrives from the sun ($\xi_{X_{opt}}$ of 41.41%). As can be sensed with Eqs. 23 and 24, such percentage of exergy loss solely depends on the optical efficiency of the mirrors, η_{field}, related to the aiming strategy selected. Since this study is undertaken for a fixed heliostat field layout, this exergy loss can only be affected by the aiming strategy of the field. The second greater exergy destruction is found in the radiative heat exchange in the tubes, X_t, involving the multiple emissions, reflections and absorptions (ξ_{X_t} of 16.84%). Given its relevance in the balance, different operation conditions will be analysed with the intent to decrease its value. The exergy destruction in the HTF, $X_{D,HTF,}$ accounts for the third greater exergy losses (4.35%) and it is affected by the internal convective coefficient, the fouling resistance and the friction of the HTF with the tube wall. Almost on a par with $X_{D,HTF}$ is the exergy loss escaping through the ambient, X_0, that depends on the heat emitted by the receiver, Q_{i0}, and the temperatures of the surfaces emitting that heat through the value of ψ_i, (Eq. 26). The percentage of exergy loss due to the external convection losses, $X_{CL,ext}$ is found to be negligible (0.69%) in comparison to the other exergy loss sources appearing. With such low value, it seems that the wind velocity modification is not a highly relevant aspect to study the exergy improvement. The exergy destruction in the absorptions and emissions in the rear wall, X_{n+1}, is just a 0.21% and the exergy loss in the tube wall, $X_{wall,t,}$ is the lower of them all, a 0.17%. This last exergy loss has been minimized in the design phase by selecting the smallest admissible thickness for the tube, according to Eq. 20.

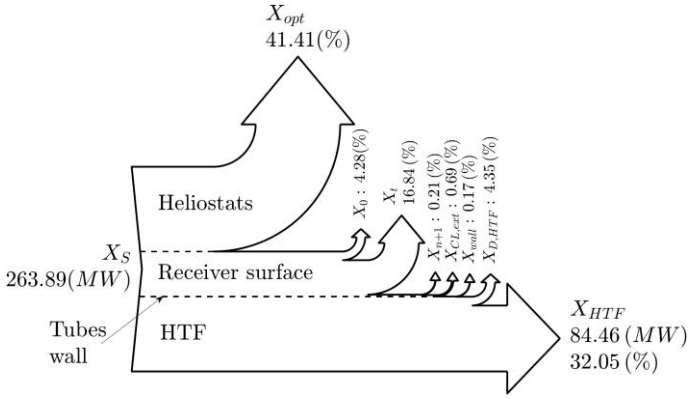

Figure 7. Sankey diagram for the exergy analysis of the receiver.

Having performed the exergy balance of the base case of study, it is then compared with scenarios of other operating conditions.

4.1. Optical properties influence

The importance of the optical properties of the coating of the tubes cannot be disregarded since they intervene in a handful of heat exchanges happening in the receiver surface. The higher the absorptivity, the lesser the radiative exergy losses will be since most of the heat received is absorbed, increasing the temperature of the surface as well, which is desirable to obtain higher exergies. Alternatively, a high emissivity and a high surface

temperature result in greater radiative losses, counteracting the benefits from the high absorptivity [10]. Nevertheless, it must be considered that these properties degrade with time [43], given the demanding conditions at which the receiver is exposed. Thus, the exergy analysis has been performed for the cases of a degradation of a 5%, 10%, 15% and 20% of the absorptivity and emissivity of the tube coating, where the nominal values (0% degradation) can be found in Table 1. The evolution of the exergy efficiency has been obtained when both the absorptivity and emissivity degrade in the same amount as well as separately (one fixed in the nominal value and the other one degrading), Figure 8.a. The same has been done for the thermal efficiency, Figure 8.b.

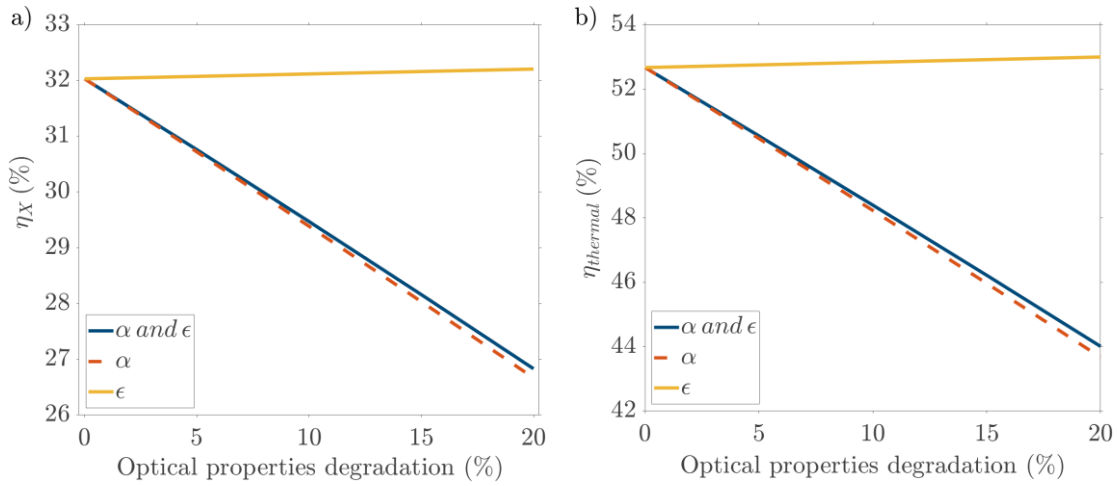

Figure 8. Evolution with the optical properties degradation of the a) exergy efficiency and b) thermal efficiency.

As expected, lower values of absorptivity lead to a slightly lesser exergy efficiency since the losses increase considerably, with a rate of over a 1% decline of the exergy efficiency every 5% of degradation of the optical properties. This highlights the need of the repainting maintenance tasks considering that, as stated by [43], the degradation rate for the Pyromark 2500 coating is in between a 0.25%/year and a 0.75%/year. It would be desirable a coating with the most stable optical behaviour as possible, as well as the higher feasible absorptivity. On the other hand, a lower emissivity results in a greater exergy efficiency, but the improvement is found to be negligible. The thermal efficiency follows the same tendency than the exergy one, although it is higher since it does not consider the temperature of the source. With the inclusion of that temperature, the exergy study constitutes an in-depth analysis that allows to observe the real possibilities for the solar energy exploitation in the receiver subsystem, analysing its different sources. Hence, it is understandable the high quantitative separation between the energy and exergy efficiencies.

The breakdown of the different percentage exergy and losses in the Eq. 34 balance is shown in Figure 9. The goal is to provide a better understanding of the evolution of the exergy efficiency, $\eta_{X,}$ with the optical properties of the tubes coating. The case of the non-degraded properties (0%) is compared with the results obtained for a combined degradation of the absorptivity and emissivity of 10% and 20%. The alternatives of isolated degradation of the absorptivity and isolated degradation of emissivity have been omitted since, as seen in Figure 8, the variation of the emissivity on its own has barely any effect respect to the initial scenario. Consequently, the degradation of just the absorptivity results

almost identical to the combined situation. Also, the intermediate scenarios of 5% and 15% of degradation are not shown since they follow the linear tendency observed between the cases of 0% degradation, 10% and 20%. The exergy loss in the heliostat field, $\xi_{X_{opt'}}$ is not presented either since it occurs upstream of the optical properties of the tubes coating modification. Also, the exergy loss in the rear wall, $\xi_{X_{n+1}}$, and in the tube wall, $\xi_{X_{wall,t}}$, have not been included since they are almost negligible (Figure 7) and are barely modified in the different alternatives studied in this Section. The exergy escaping the receiver through surface *0* (the ambient), ξ_{X_0}, is presented divided into the components mentioned in Section 2.3, $\xi_{X_{0,refle}}$ and $\xi_{X_{0,emi}}$, to get a better sense of the influence that the optical properties have on them.

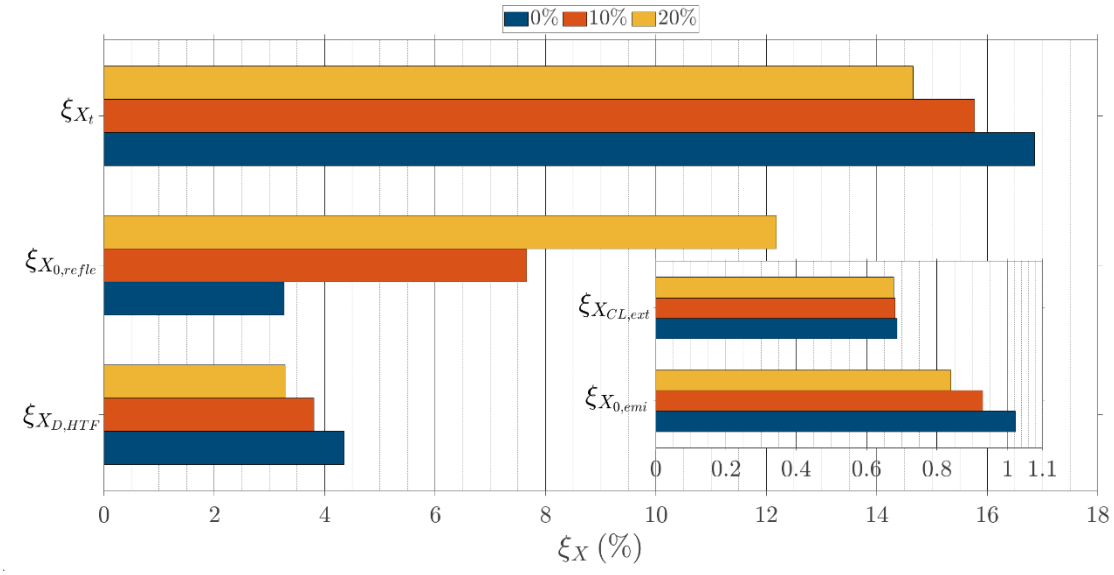

Figure 9. Breakdown of the percentage exergies evolution with the optical properties degradation.

This representation of the different percentage exergies shows that the exergy destruction due to the radiation heat absorbed by the tubes, ξ_{X_t}, decreases with the absorptivity degradation of their coating over a 2%. Such lesser absorptivity is translated in a lower heat absorbed by the tubes, decreasing the wall temperature as it "retains" less heat. It means then that the heats exchanged between surfaces (Eq. 4) are lesser since lower temperature values of the surfaces mean less emission (Eq. 1). Looking at the X_t exergy loss term (Eq. 27), the lower temperatures as well as emission and heat exchanged between surfaces, although not being extreme cases, result in a notable descend of this exergy loss. On the other hand, the exergy loss of radiation heat to the ambient, $\xi_{X_{0'}}$ increases. In that ξ_{X_0}, the most relevant increment (of over a 9%) takes place for the exergy destruction due to the radiation heat escaping through the ambient that initially entered the receiver system through the ambient as well, $\xi_{X_{0,refle}}$. Thus, it is radiation heat that has only been reflected by the tubes and/or rear wall but not absorbed by them. Again, its increment is motivated by the degradation of the absorptivity (which implies a greater reflectivity), affecting the temperatures distribution on the tubes and the heats exchanged, modifying the result of the product $\psi_i Q_{ij}$ (Eq. 26). On the other hand, the exergy escaping also through the ambient, but originated from the emissions of the tubes and rear wall, $\xi_{X_{0,emi}}$, is smaller than the former

one, being that difference even more notable with the optical properties degradation, since the emissivity decreases. Hence, most of the exergy leaving to the ambient has its origin in the ambient itself. Summing up, the temperature of the tube wall decreases since the radiation losses are greater, being closer to the HTF temperature. Thus, the exergy losses due to convection and due to the heat conduction in the tube wall both decrease as well. Moreover, the temperature in the tube inner wall, T_{film}, is more similar to the HTF temperature, which also explains the descend of $\xi_{X_{D,HTF}}$. The exergy efficiency decreases considerably the greater the optical properties degradation is even though the entropy generation is also lower, which means that the heat reaching the fluid is also lesser. As seen in the breakdown, that descend in the heat transferred to the HTF is due to the greater $X_{0,refle}$.

4.2. Aiming strategy and DNI influence

The effect of the DNI level modification, from 550 Wm^{-2} to 1000 Wm^{-2}, in the exergy efficiency has been studied for the base case. It would be equivalent to a change in location or the variation in the number of mirrors in the heliostat field and it results in a modification of the HTF velocity (and therefore its mass flow). The base configuration has been tested under a peak aiming of the heliostat field as well. An instance of the peak distribution at a DNI of 930 Wm^{-2} (the same one that was initially considered for the base case with flat aiming) is depicted in Figure 10. This peak aiming provides a maximum heat flux of 1.5 MW m^{-2}, opposite to the maximum of 1.2 MW m^{-2} found in the flat aiming strategy (Figure 5), as well as a much narrow area of maximum values of such incident heat flux on the receiver.

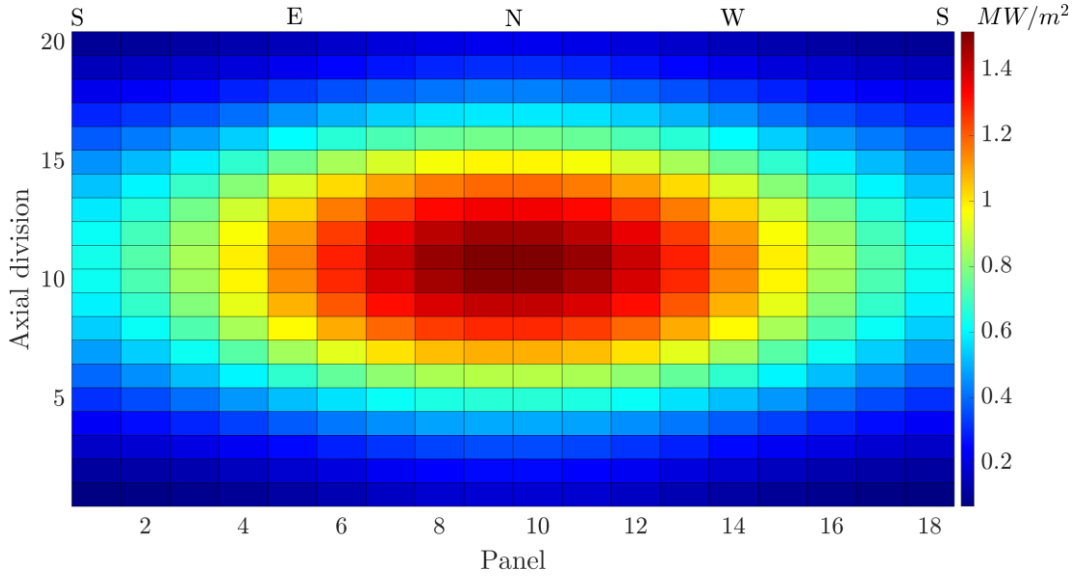

Figure 10. Discretized heat flux distribution on the receiver surface with the peak aiming strategy.

The temperature distribution in the outer tube wall presents the same tendency than the corresponding heat flux in each strategy. Figure 11 gives a better sense of the differences in the temperature distribution on the outer tube wall resulting from both strategies. The temperature evolution through the axial divisions for a fixed circumferential position (θ=0°), is depicted in Figure 11.a. As can be seen, the peak aiming reaches higher temperatures at the middle of each panel (*h=10, 30…*) as well as a lesser homogeneous

temperature in *z*: the temperature gradient between the middle of the panels, i.e. *h=10*, and its ends, i.e. *h=20*, is greater than in the flat aiming. The peak aiming strategy gives a maximum temperature of 752.8 °C while the flat one results in 678.1 °C. On the other hand, Figure 11.b provides the temperature evolution in θ for the tenth axial division, showing that the rear half of the tubes is at almost the same temperature with both aiming strategies. However, the front side of them is at greater temperatures in the peak configuration. Thus, the circumferential gradient for the peak case is around 433°C, opposite to the 347 °C of the flat one. The understating of how both tube outer temperature distributions diverge, while the HTF temperature remains the same in the two cases, will ease the comprehension of the different exergy losses.

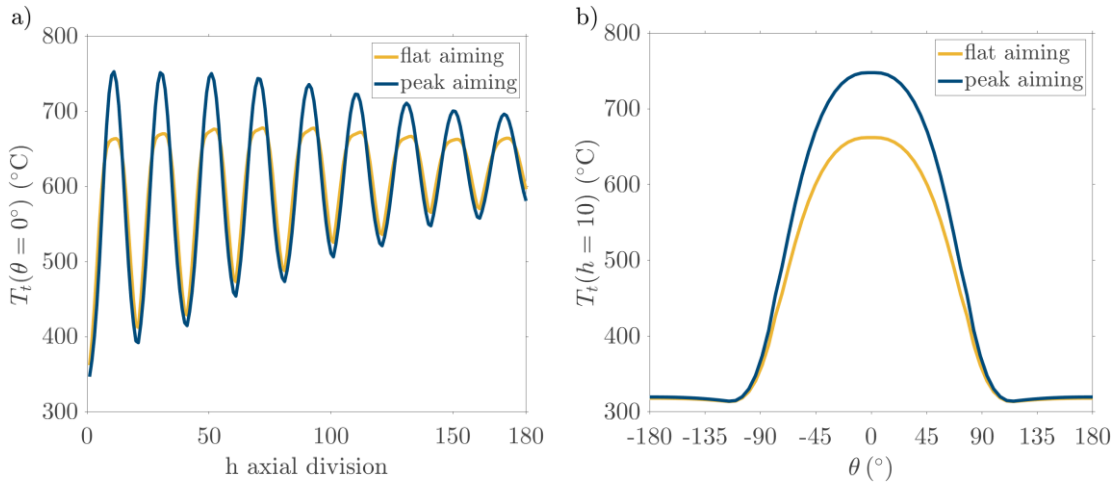

Figure 11. a) Axial evolution of the tube wall temperature at *θ=0°* and b) circumferential evolution of the tube wall temperature at *h=10*.

It can be seen in Figure 12 that the exergy efficiency grows when the DNI level increases. This tendency is observed for the peak and flat cases, showing also a reduction of the efficiency growth rate (gradient) when the DNI moves to greater levels. Between the two aiming strategies, the peak one provides the greater exergy efficiency. However, it should be considered that the non-homogenization of the incident flux on the receiver obtained with the peak aiming strategy leads to excessively high temperatures at some spots of the tubes as well as circumferential gradients, resulting in greater thermal and mechanical stresses. Hence, the structural limits of the receiver need to be watched to ensure the correct operation of the receiver during the lifetime projected for the SPT plant. On the other hand, just as happened in Section 4.1, the thermal efficiency is greater than the exergy one.

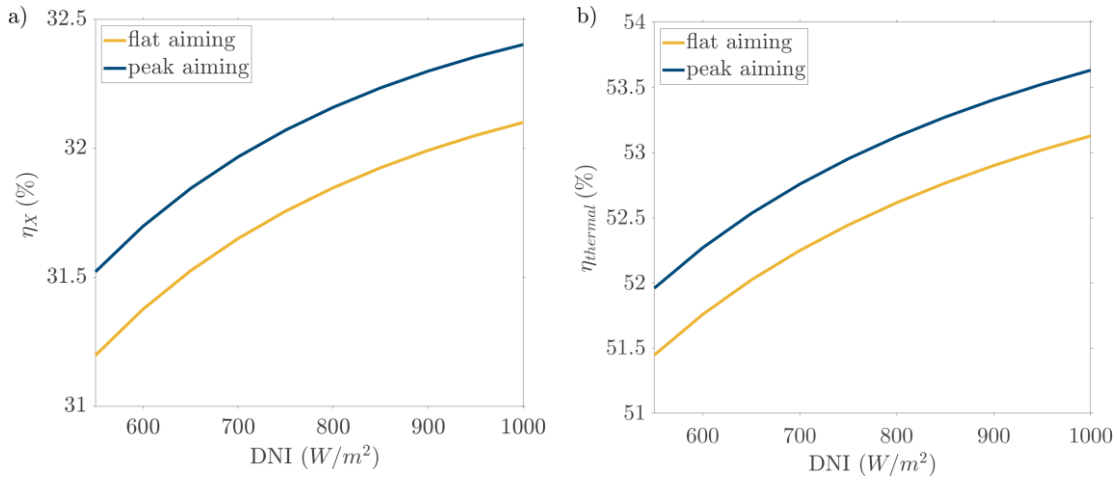

Figure 12. Evolution, for flat and peak aiming strategies and different DNI levels, of the a) exergy efficiency and the b) thermal efficiency.

The breakdown for the percentage of the exergy losses of Eq. 34 is also shown for this DNI and aiming modification study, Figure 13. For a fixed DNI, the exergy from the Sun, X_S, is the same regardless the aiming since both cases have the same field layout. Regarding the main discrepancies between the flat and peak aiming strategies observed in the percentage dissection, the flat one presents a higher exergy destruction in the heliostat field, $\xi_{X_{opt}}$. Such outcome is due to the lesser mirrors efficiency, η_{field}, respect to the peak aiming caused by the greater spillage losses, as a result of going for a more homogeneous heat flux distribution on the receiver surface, especially in the axial direction. Thus, the heat arriving from the heliostat field to the receiver is greater in the peak alternative, being the option with the greater HTF mass flow as well, around a 1.35% in all of the DNI scenarios.

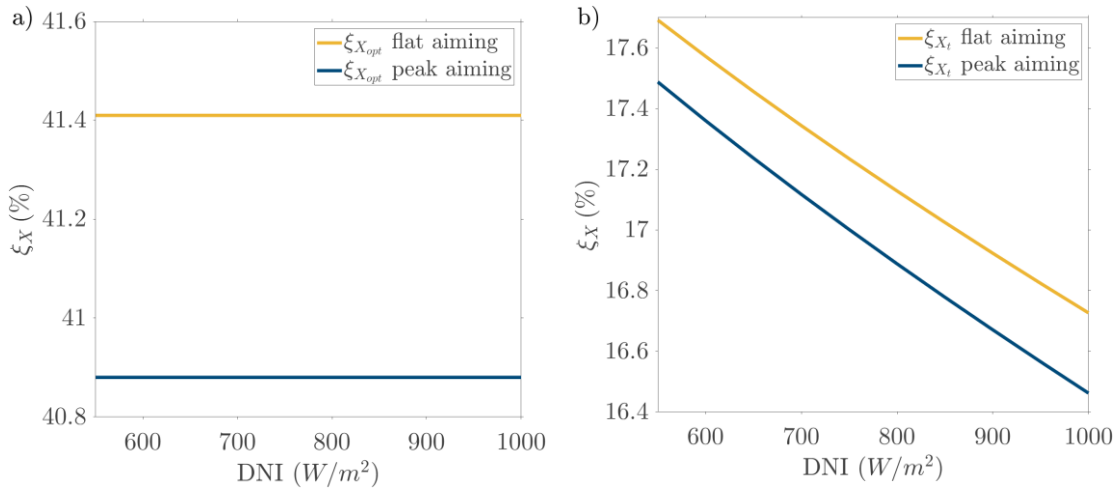

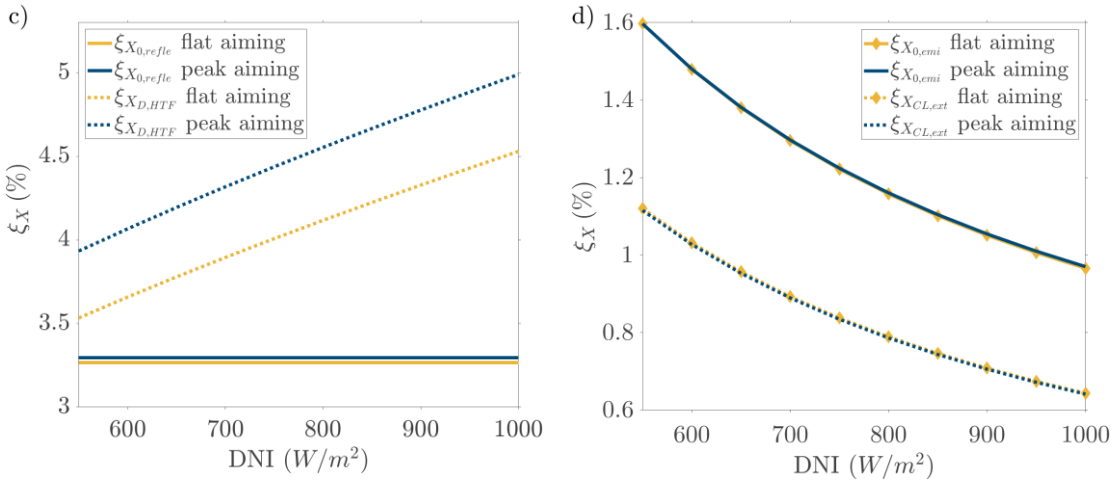

Figure 13. Breakdown of the percentage exergies evolution with the DNI for flat and peak aiming strategies.

The exergy destruction due to the tube radiation heat absorption, ξ_{X_t}, is greater again for the flat aiming scenario. Looking at the terms in Eq. 27, there are contradictory effects between them that eventually lead to the result obtained for this loss. The lesser radiation reaching the receiver in the flat case (see Figures 5 and 10) contributes to a temperature profile with lower values. It is also more homogeneous and does not present excessively hot spots in the flat configuration, opposite to the peak one, where the aiming leads to a highly uneven temperature distribution (see Figure 11). The emissivity E_i and heat exchanged by the surfaces Q_{ij} presents the same tendency in the two configurations, both qualitative and quantitative but, in this case, the quantitative differences are tiny. On the other hand, the maximum efficiency ratio, ψ_i, is found to be overall greater for the flat aiming. Moving on, the flat aiming alternative has a lesser exergy destruction in the heat transfer from the inner tube wall to the HTF, $\xi_{X_{D,HTF}}$, precisely due to the lower overall temperature distribution; such descend in the tube outer temperature affects also the tube inner wall temperature, lessening the temperature gradient between the tube inner wall and the HTF, since the latter presents virtually the same temperature profile evolution through the receiver in both configurations. Also, the heat Q_{abs} is slightly higher in the peak case since more HTF mass flow rate circulates through the tubes. Thus, the first two exergy destruction sources mentioned are the ones responsible for the lesser exergy efficiency in the combined operation of the heliostat field and the receiver when using the flat aiming strategy in comparison to the peak one. Meanwhile, the exergy loss in the HTF plays in favour of the flat aiming configuration. In addition, both components of ξ_{X_0}, $\xi_{X_{0,refle}}$ and $\xi_{X_{0,emi}}$, as well as $\xi_{X_{CL,ext}}$ are almost identical for these two strategies, as depicted in Figures 13.c and 13.d. Looking at the exergy efficiency expression (Eq. 33), the greater heat absorbed by tubes in the peak aiming scenario as well as the higher temperatures of the tube wall contribute to a better performance of the peak alternative. The total entropy generated, although greater (4.498×10^4 W K^{-1} opposite to 4.0822×10^4 W K^{-1}), is not enough to counteract such previously mentioned advantages gained from the heat absorbed and tube wall temperature. The greater entropy generation is found in the temperature gradient between the inner tube wall and the HTF, being one order of magnitude greater than the entropy generated in the tube wall conduction and three orders of magnitude greater than the one due to the pressure drop.

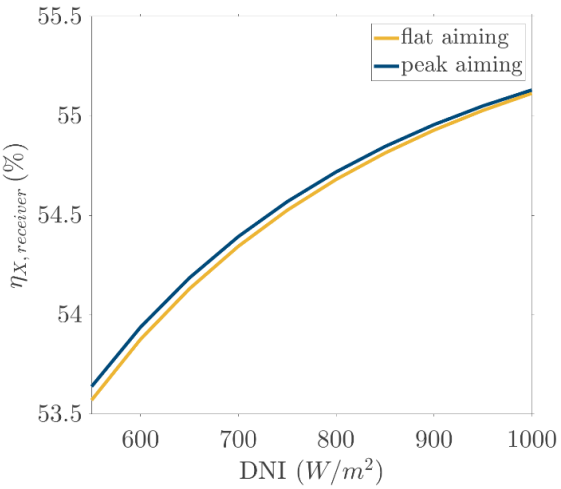

Figure 14. Exergy efficiency of the SPT receiver for flat and peak aiming strategies under different DNI.

Given the great difference observed in the exergy loss due to the heliostat field, $\xi_{X_{opt}}$, between both aimings, the exergy efficiency of just the receiver is depicted in Figure 14. This would be the exergy gain in the HTF over the exergy arriving from the heliostat field: $\eta_{X,receiver} = 100\frac{X_{HTF}}{X_S - X_{opt}}$. Such Figure highlights that the receiver on its own is virtually independent from the aiming strategy selected: the improvements in the exergy losses from one aiming option are counteracted by a poorer performance of other of its losses. For instance, in the peak aiming case, the higher $\xi_{X_{D,HTF}}$ with respect the flat one is compensated with the lesser ξ_{X_t}. However, the strategy is indeed relevant for the whole plant, as seen for the global η_X, that considers the heliostat field as well (Figure 12), making the $\xi_{X_{opt}}$ the defining factor that cannot be disregarded by only analysing the receiver exergy efficiency.

4.3. Ambient temperature influence

Until now, the ambient temperature has not been considered, remaining fixed regardless the DNI, showing an improvement in the exergy efficiency with the higher the DNI. However, the surroundings temperature is not decoupled from the DNI and is indeed a relevant factor in the exergy analysis: as mentioned earlier, lower surroundings temperatures result in greater exergies since the ability of a substance or process to produce work lasts until it is in thermal equilibrium with the ambient. It can be observed from multiple meteorological data that an increase of the DNI at a certain location comes with a growth of the ambient temperature. Thus, the increase of the exergy efficiency associated with a higher DNI may be counteracted if the surroundings temperature increases enough. With all of this, Figure 15 provides the evolution of the exergy efficiency with the DNI level for different ambient temperatures. The aiming strategy is the flat one, as selected for the base case. On the other hand, the thermal efficiency, depicted earlier in Figure 12.b remains unchanged regardless the surroundings temperature so it is not the best indicator to compare different locations.

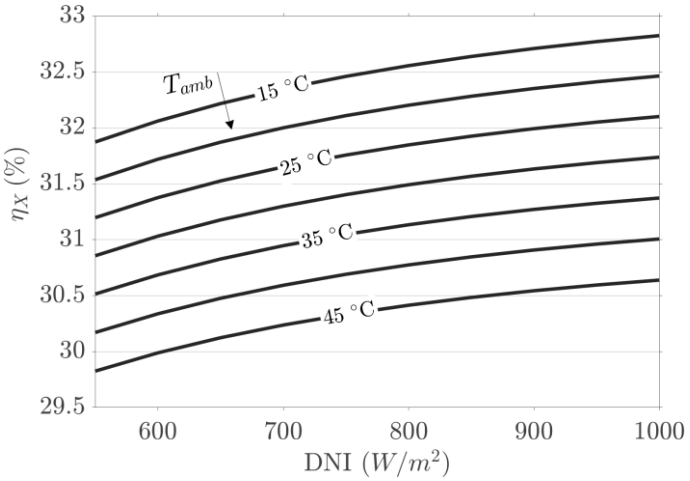

Figure 15. Exergy efficiency evolution with the DNI for different ambient temperatures.

As expected, the isothermals follow a decreasing tendency the greater the ambient temperature is and its relevance in the exergy efficiency is not negligible. Then, for instance, it is preferable in terms of exergy efficiency a location with a DNI of 800 W m^{-2} and an average surroundings temperature of 25 °C rather than another with a DNI of 900 W m^{-2} and an average surroundings temperature of 30 °C. The goal should be finding a location with a moderate/high average DNI level and the lowest ambient temperature as possible. Moreover, lower DNI results in lower tube wall temperatures, relaxing the thermal stress. Meanwhile, for a fixed DNI level, the tube wall temperature distribution is virtually the same regardless the surroundings temperature, with the tiny divergences being due to the higher convection losses with lower ambient temperatures.

A good instance of low ambient temperatures and low/moderate DNI would be the location of the PROMES laboratories, at the French side of the Pyrenees. The 1500 m altitude of the location favours its low average temperatures, with the coldest months having average maximum temperatures around 4 °C and average maximum DNI over 450 W m^{-2} and the hottest ones with average temperatures between 13 and 20 °C and average maximum DNI around 650 W m^{-2}. Particularly interesting is the case of Ouarzazate, in the Moroccan dessert, with average maximum temperatures of around 17 °C in winter and DNI over 850 W m^{-2}. However, during the summer months, the maximum average DNI is around 800 W m^{-2} and temperatures reach up to 38 °C. Examples of high surroundings temperatures and high DNI would be the location of the Ashalim SPT plant, at Israel, or the Crescent Dunes SPT plant at Nevada, US, both placed at warm and arid regions. The worst case presented for PROMES (during its summer months) resembles to the best scenarios for these locations, occurring in winter. However, in summer, temperatures over 30 °C and DNI of over 830 W m^{-2} are typically reached. Almost 900 W m^{-2} can be reached in August at Crescent Dunes. Lastly, Noor Energy 1, at Dubai presents moderate DNI, with an average value of around 730 W m^{-2}, influenced by its dusty location. On the other hand, it suffers from extremely high temperatures, ranging from maximum average temperatures of 23 °C in winter to maximum average temperatures over 40 °C in summer, given its proximity to the equatorial line. The meteorological data commented has been obtained from [44].

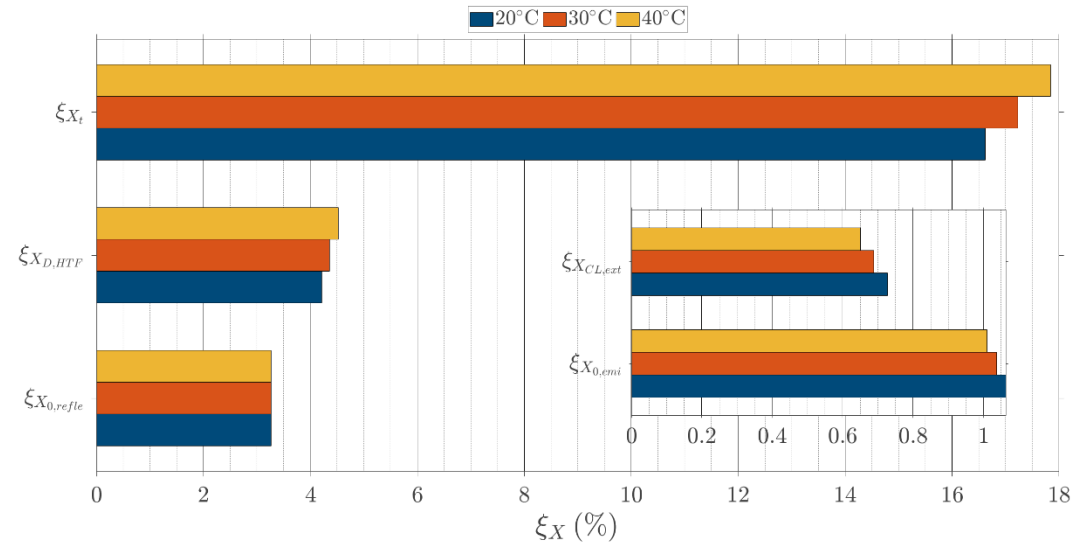

Figure 16. Breakdown of the percentage exergies evolution with the DNI for different ambient temperatures.

The breakdown for the percentage exergy losses is depicted in Figure 16 for different ambient temperature under the flat aiming strategy scenario. Since the evolution with the DNI of the different losses has already been depicted in Figure 13 for flat aiming and 25 °C, and given that it is the same for the rest of the ambient temperatures, only the results for a DNI of 900 W m^{-2} are shown. The biggest difference between the cases is the exergy loss due to the radiation heat absorbed by the tubes, that grows greatly with the ambient temperature. The same thing happens with the exergy destruction due to the internal convection in the HTF and friction with the tube wall, although the differences are not that big. The losses $\xi_{X_{0,refle}}$ remain the same regardless the ambient temperature, while the losses $\xi_{X_{0,emi}}$ increase slightly with the surroundings temperature, as well as $\xi_{X_{CL,ext}}$, although they can be considered negligible. Thus, the two main sources of exergy losses are also the ones suffering from the greater growth with the ambient temperature. The maximum efficiency ratio, ψ (Eq. 21), decreases with the surroundings temperature, which makes the $\xi_{X_{0,emi}}$ diminish as well since it has a direct dependence with it (Eq. 26). The reduction of $\xi_{X_{CL,ext}}$ can be explained by looking at Eq. 29, where the term $1\text{-}T_{ref}/T_j$ decreases the higher the ambient temperature. The convective losses are diminished as well the higher the ambient temperature is, but the differences obtained for one surroundings temperature or the other are quite small. On the other hand, $\xi_{X_{wall,t}}$ and $\xi_{X_{D,HTF}}$ have a direct dependence on the ambient temperature (Eqs. 30 and 31), while ξ_{X_t} (Eq. 28) presents the combination of the term $1\text{-}T_{ref}/T_j$ and the maximum efficiency ratio, resulting in a greater loss the higher the temperature.

5. Conclusions

A method to obtain the different exergies present in the SPT plants, from the heliostat field to the receiver subsystem, has been introduced. The present analysis considers the circumferential thermal gradients in the receiver tubes, providing an accurate solution to a problem so highly sensitive to the temperature of the surfaces involved. Prior the exergy analysis, the thermal resolution of the receiver also takes into account the structural limits

of the material selected for the tubes, in terms of pressure and corrosion, in order to minimize the entropy generation through the tube wall by selecting the lower thickness admissible.

With the method showcased, the exergy analysis has been performed for a typical receiver configuration, resulting in an exergy efficiency of 32.5%. The heliostat field exergy destruction, $\xi_{X_{opt}}$ is found to be the most prominent exergy loss, being a 41.41%. However, for a fixed field layout, its value can only be altered with the modification of the aiming strategy, regardless the ambient conditions and receiver design. Such outcome is due to mirrors efficiency because of the spillage losses: the strategies going for a more homogeneous heat flux distribution on the receiver surface suffering from greater spillage than those showing greater flux peaks. Regarding the receiver, the exergy loss due to the emissions and absorptions in the tubes, ξ_{X_t}, is the greatest (16.84% in this configuration), followed by the ones due to the internal heat transfer convection, fouling resistance and friction of the HTF with the tube walls, $\xi_{X_{D,HTF}}$ (4.35%). Both are highly dependent on the tube walls temperature distributions. As for the heat escaping through the ambient, ξ_{X_0}, its value is quite similar to $\xi_{X_{D,HTF}}$ in this case, a 4.28%. its dissection shows that it is mainly due to heat coming from the ambient and being reflected back to it (around two thirds), with the heat emitted by the tubes and rear wall resulting less relevant. The effects of the external convection and the influence of the rear wall are considerably lesser than the rest, being 0.69% and 0.21% respectively. The exergy destruction due to the tube wall conduction was minimized by selecting the minimum admissible thickness, resulting in just a 0.17%.

In order to get a better sense of the importance of the different exergy losses present in the balance, several parameters were varied with respect the original case. Although great exergy efficiency divergences were not expected due to the non-modification of the two focal temperatures (the Sun temperature and the HTF one), various conclusions regarding the individual exergy losses sources were reached. It has been seen that with the degradation of the optical properties of the coating, which is an inevitable phenomena happening in this kind of receivers due to the demanding thermal conditions, the exergy efficiency drops over a 1% every 5% of the degradation of the optical properties. Also, the effects of the absorptivity have been proven to be more relevant than the ones of the emissivity, that barely counteracts the former one. The variation of the absorptivity alone dropped the exergy efficiency from the initial 32.05% to around less than a 27% in the worst case studied (20% degradation), while the modification of the emissivity alone resulted in an exergy efficiency of 32.2%, providing an improvement of just a 0.15%. Hence, it is concluded that the efforts when selecting the coating must focus on the absorptivity and not so much on the emissivity and repainting tasks may be needed over time if the coating material, which typically degrades between a 0.25%/year and 0.75%/year, is not stable enough during the plant lifecycle. Regarding the aiming strategy, the peak alternative is the one with the greater exergy efficiency, despite the greater entropy generation through the tube wall, around a 0.45% greater than in the flat case. This is almost compensated with the improvement of ξ_{X_t} for the peak aiming over the flat (around 0.23%), resulting in exergy efficiencies almost similar when looking just the receiver. Thus, the difference made by the optical efficiency of the heliostat field is determinant to favour the peak configuration since

constitutes a lower exergy loss by itself (40.88% instead of 41.41%) while also providing a greater heat flux to the receiver. However, structural limits should be considered when resorting to these highly aggressive alternatives. Moving on, higher levels of DNI result in greater exergy efficiencies, but the effect of the site temperature should not be disregarded, making more attractive locations with moderately high DNI and lower ambient temperatures over those with the higher DNI and higher surroundings temperatures associated. In this case, the exergy efficiency provides answers over the thermal efficiency, since the latter is not affected by the ambient temperature of the location. For a fixed DNI level, an increase of 5 °C in the ambient temperature results in a drop of over a 0.35% in the exergy efficiency, being the divergences more notable when comparing different DNI and surroundings temperature combinations.

Acknowledgements

This research is partially funded by the scholarship "Ayudas para la formación del profesorado universitario" (FPU-02361) awarded by the Spanish Ministerio de Educación, Cultura y Deporte (MECD), the fellowship "Ayuda a la investigación en energía y medio ambiente" of the Iberdrola España Foundation, the Spanish government under the project RTI2018-096664-B-C21 (MICINN/FEDER, UE) and the call "Programa de apoyo a la realización de proyectos interdisciplinares de I+D para jóvenes investigadores de la Universidad Carlos III de Madrid 2019-2020", under the frame of the Convenio Plurianual Comunidad de Madrid- Universidad Carlos III de Madrid.

References

[1] Masson-Delmotte V, Zhai P, Pörtner H-O, Roberts D, Skea J, Shukla PR, et al. Global Warming of 1.5°C. An IPCC Special Report on the impacts of global warming of 1.5°C above pre-industrial levels and related global greenhouse gas emission pathways, in the context of strengthening the global response to the threat of climate change,. 2018.

[2] IRENA. Global energy transformation: A roadmap to 2050 (2019 edition). 2019.

[3] IRENA. Renewable energy statistics 2018. 2018.

[4] Qiu Z, Li P. Advanced Energy Efficiency Technologies for Solar Heating, Cooling and Power Generation. Cham: Springer International Publishing; 2019. https://doi.org/10.1007/978-3-030-17283-1.

[5] IRENA. Renewable Energy Cost Analysis: Concentrating Solar Power. International Renewable Energy Agency. vol. 1. 2012.

[6] IRENA. The Power to Change: Solar and Wind Cost Reduction Potential to 2025. 2016.

[7] Lilliestam J, Labordena M, Patt A, Pfenninger S. Empirically observed learning rates for concentrating solar power and their responses to regime change. Nat Energy 2017;2. https://doi.org/10.1038/nenergy.2017.94.

[8] Petela R. Exergy analysis of the solar cylindrical-parabolic cooker. Sol Energy 2005;79:221–33. https://doi.org/10.1016/j.solener.2004.12.001.

[9] Petela R. Exergy of Heat Radiation. J Heat Transfer 1964;86:187–92. https://doi.org/doi.org/10.1115/1.3687092.

[10] Petela R. Exergy of undiluted thermal radiation. Sol Energy 2003;74:469–88.

https://doi.org/10.1016/S0038-092X(03)00226-3.

[11] Candau Y. On the exergy of radiation. Sol Energy 2003;75:241–7. https://doi.org/10.1016/j.solener.2003.07.012.

[12] Bejan A. Second-Law Analysis in Heat Transfer and Thermal Design. Adv Heat Transf 1982;15:1–58. https://doi.org/10.1016/S0065-2717(08)70172-2.

[13] Flesch J, Marocco L, Fritsch A, Niedermeier K, Wetzel T. Entropy Generation Minimization Analysis of Solar Salt, Sodium, and Lead–Bismuth Eutectic as High Temperature Heat Transfer Fluids. J Heat Transfer 2020;142:1–10. https://doi.org/10.1115/1.4046302.

[14] Öztürk HH. Experimental determination of energy and exergy efficiency of the solar parabolic-cooker. Sol Energy 2004;77:67–71. https://doi.org/10.1016/j.solener.2004.03.006.

[15] Cocco D, Petrollese M, Tola V. Exergy analysis of concentrating solar systems for heat and power production. Energy 2017;130:192–203. https://doi.org/10.1016/j.energy.2017.04.112.

[16] Padilla RV, Fontalvo A, Demirkaya G, Martinez A, Quiroga AG. Exergy analysis of parabolic trough solar receiver. Appl Therm Eng 2014;67:579–86. https://doi.org/10.1016/j.applthermaleng.2014.03.053.

[17] Bellos E, Tzivanidis C. A detailed exergetic analysis of parabolic trough collectors. Energy Convers Manag 2017;149:275–92. https://doi.org/10.1016/j.enconman.2017.07.035.

[18] Bellos E, Tzivanidis C. Alternative designs of parabolic trough solar collectors. Prog Energy Combust Sci 2019;71:81–117. https://doi.org/10.1016/j.pecs.2018.11.001.

[19] Kumar A, Sharma M, Thakur P, Thakur VK, Rahatekar SS, Kumar R. A review on exergy analysis of solar parabolic collectors. Sol Energy 2020;197:411–32. https://doi.org/10.1016/j.solener.2020.01.025.

[20] Pye J, Zheng M, Asselineau C, Coventry J. An exergy analysis of tubular solar-thermal receivers with different working fluids. Int. Conf. Conc. Sol. Power Chem. Energy Syst. (SolarPACES 2014), Beijing, 2014.

[21] Asselineau C-A, Coventry J, Pye J. Exergy analysis of the focal-plane flux distribution of solar-thermal concentrators. Appl Energy 2018;222:1023–32. https://doi.org/10.1016/j.apenergy.2018.04.027.

[22] Gómez-Hernández J, González-Gómez PA, Briongos J V., Santana D. Influence of the steam generator on the exergetic and exergoeconomic analysis of solar tower plants. Energy 2018;145:313–28. https://doi.org/10.1016/j.energy.2017.12.129.

[23] Novales D, Erkoreka A, De la Peña V, Herrazti B. Sensitivity analysis of supercritical CO2 power cycle energy and exergy efficiencies regarding cycle component efficiencies for concentrating solar power. Energy Convers Manag 2019;182:430–50. https://doi.org/10.1016/j.enconman.2018.12.016.

[24] Hernández-Jiménez F, Soria-Verdugo A, Acosta-Iborra A, Santana D. Exergy recovery from solar heated particles to supercritical CO2. Appl Therm Eng 2019;146:469–81. https://doi.org/10.1016/j.applthermaleng.2018.10.009.

[25] Kouta A, Al-Sulaiman F, Atif M, Marshad S Bin. Entropy, exergy, and cost analyses of solar driven cogeneration systems using supercritical CO2 Brayton cycles and MEE-

TVC desalination system. Energy Convers Manag 2016;115:253–64. https://doi.org/10.1016/j.enconman.2016.02.021.

[26] Rodríguez-Sánchez MR, Soria-Verdugo A, Almendros-Ibáñez JA, Acosta-Iborra A, Santana D. Thermal design guidelines of solar power towers. Appl Therm Eng 2014;63:428–38. https://doi.org/10.1016/j.applthermaleng.2013.11.014.

[27] Sánchez-González A, Rodríguez-Sánchez MR, Santana D. Aiming factor to flatten the flux distribution on cylindrical receivers. Energy 2018;153:113–25. https://doi.org/10.1016/j.energy.2018.04.002.

[28] Berger X, Buriot D, Garnier F. About the equivalent radiative temperature for clear skies. Sol Energy 1984;32:725–33. https://doi.org/10.1016/0038-092X(84)90247-0.

[29] Siebers D, Kraabel J. Estimating convective energy losses from solar central receivers. Albuquerque, NM, and Livermore, CA (United States): 1984. https://doi.org/10.2172/6906848.

[30] Romeo E, Royo C, Monzón A. Improved explicit equations for estimation of the friction factor in rough and smooth pipes. Chem Eng J 2002;86:369–74. https://doi.org/10.1016/S1385-8947(01)00254-6.

[31] Gnielinski VV. Neue Gleichungen für den Wärme- und Stoffaustausch in turbulent durchströmten Rohren und Kanälen, Forsch. Ing. Wes. 41 (1) (1975) 8–16. Englisch Translation: New equations for heat and mass transfer in turbulent pipe and channel flow,. Int Chem Eng 1976;16:359–68.

[32] Idel'chik IE. Handbook of hydraulic resistance. 3rd ed. New York, USA: Begell House; 1960.

[33] American Society of Mechanical Engineers, ASME Boiler and Pressure Vessel Code 2013.

[34] Bejan A. General criterion for rating heat-exchanger performance. Int J Heat Mass Transf 1978;21:655–8. https://doi.org/10.1016/0017-9310(78)90064-9.

[35] Tian Y, Zhao CY. A review of solar collectors and thermal energy storage in solar thermal applications. Appl Energy 2013;104:538–53. https://doi.org/10.1016/j.apenergy.2012.11.051.

[36] Conroy T, Collins MN, Grimes R. A review of steady-state thermal and mechanical modelling on tubular solar receivers. Renew Sustain Energy Rev 2020;119. https://doi.org/10.1016/j.rser.2019.109591.

[37] Zavoico AB. Solar Power Tower - Design Basis Document. Tech Rep SAND2001-2100 2001:148. https://doi.org/10.2172/786629.

[38] Rodriguez-Sanchez MR, Sanchez-Gonzalez A, Marugan-Cruz C, Santana D. Flow patterns of external solar receivers. Sol Energy 2015;122:940–53. https://doi.org/10.1016/j.solener.2015.10.025.

[39] McConohy G, Kruizenga A. Molten nitrate salts at 600 and 680°C: Thermophysical property changes and corrosion of high-temperature nickel alloys. Sol Energy 2014;103:242–52. https://doi.org/10.1016/j.solener.2014.01.028.

[40] Ho CK, Mahoney AR, Ambrosini A, Bencomo M, Hall A, Lambert TN. Characterization of Pyromark 2500 for High-Temperature Solar Receivers. ASME 2012 6th Int. Conf. Energy Sustain. Parts A B, vol. 136, American Society of Mechanical Engineers; 2012,

p. 509–18. https://doi.org/10.1115/ES2012-91374.

[41] Wade WR, Slemp WS. Measurements of total emittance of several refractory oxides, cermets, and ceramics for temperatures from 600 degrees F to 2,000 degrees F (no. TN-D-998). Washington DC: 1962.

[42] Scannapieco JF. Irradiation of thermal control coatings, Final report. NASA-CR-94684, DOC.-68SD4224. 1968.

[43] Ho CK, Pacheco JE. Levelized Cost of Coating (LCOC) for selective absorber materials. Sol Energy 2014;108:315–21. https://doi.org/10.1016/j.solener.2014.05.017.

[44] European Commision. Photovoltaic geographical information system. https://re.jrc.ec.europa.eu/pvg_tools/en/tools.html (accessed June 10, 2020).